Alexandria Engineering Journal (2022) 61, 7393–7415

Alexandria University

Alexandria Engineering Journal

www.elsevier.com/locate/aej
www.sciencedirect.com

Numerical investigation of nanofluid mixed convection in a T-shaped cavity by considering a thermal barrier

Simon Xia [a,*], Mohammad Mostafavi [b], Tawfeeq Alghazali [c], Sajad sadi [d], John William Grimaldo Guerrero [e], Wanich Suksatan [f], Davood Toghraie [b,*], Afrasyab Khan [g]

[a] *College of Mechanical Engineering, Yancheng Institute of Technology, Yancheng, Jiangsu, 224051, China*
[b] *Department of Mechanical Engineering, Khomeinishahr Branch, Islamic Azad University, Khomeinishahr, Iran*
[c] *Director of Islamic university in Najaf, Iraq*
[d] *Department of mechanical engineering, Imam Hossein Comprehensive University, Iran*
[e] *Departamento de Energía, Universidad de la Costa, Barranquilla, Colombia*
[f] *Faculty of Nursing, HRH Princess Chulabhorn College of Medical Science, Chulabhorn Royal Academy, Bangkok 10210, Thailand*
[g] *Research Institute of Mechanical Engineering, Department of Vibration Testing and Equipment Condition Monitoring, South Ural State University, Lenin prospect 76, Chelyabinsk 454080, Russian Federation*

Received 6 April 2021; revised 10 November 2021; accepted 1 January 2022
Available online 15 January 2022

KEYWORDS

Heat transfer;
Mixed convection;
Nanofluid;
Mixture model;
Cavity;
Richardson number

Abstract In this study, the numerical investigation of Al_2O_3-Water nanofluid mixed convection in a T-shaped lid-driven cavity in the presence of a thermal barrier with positioning at different positions is investigated by the two-phase mixture model. Variable parameters in this study are the cavity aspect ratio (AR), the volume fraction of nanoparticles (ϕ), Richardson numbers (Ri), and different thermal barrier placements in the cavity. The results indicated that the increase in the Richardson number leads to an increase in the local and average Nusselt number (Nu_{ave}) and heat transfer. Increasing the ϕ also increases the heat transfer while increasing the aspect ratio decreases the heat transfer. Regarding the geometrical position of the thermal barrier, the results show that the geometrical position of the thermal barrier near the lid has the highest heat transfer and the Nusselt number. Numerical investigation of nanofluid mixed convection in a T-shaped cavity by considering a thermal barrier is the originality of this work.

1. Introduction

Nanostructures are very important in many applications of engineering, technology and natural processes [1–6]; among

* Corresponding authors.
E-mail addresses: jasonxia88@yeah.net (S. Xia), davoodtoghraie@iaukhsh.ac.ir (D. Toghraie).
Peer review under responsibility of Faculty of Engineering, Alexandria University.

https://doi.org/10.1016/j.aej.2022.01.009

Nomenclature

$\vec{V}$	velocity [m/s]
g	gravity [m/s^2]
T	temperature [K]
AR	aspect ratio
L	length [m]
k	thermal conductivity [W/m.K]
Nu	Nusselt number
Gr	Grashof number
Ri	Richardson number
f_{drag}	drag function
X	dimensionless longitudinal component
Y	dimensionless transverse component
x	longitudinal component [m]
y	transverse component [m]

Greek symbols

ϕ	volume fraction
ρ	density [kg/m^3]
β	thermal expansion coefficient [1/K]
μ	viscosity [Pa.s]

Abbreviations

f	fluid
p	particle
eff	effective
h	hot
c	cold
loc	local
ave	average
m	mixture
k	kth phase
lid	lid-driven
dr	drift

these applications, these applications include cooling systems that are used today in industries such as power generation, transportation and electronics. Nanofluids can be used to achieve greater heat transfer [7–17]. In recent decades, a lot of research was done on nanofluids [18], MEMS [19], and structural, morphological and optical properties of nanosttructures [20–23]. Their research showed that the Richardson number was the cause of the increase in heat transfer. Mirmasoumi and Behzadmehr [24] investigated the heat transfer of nanofluid in a cavity. They showed that the convective heat transfer coefficient increases with decreasing nanoparticle's diameter. Aminossadati and Ghasemi [25] conducted a numerical study of mixed convection in an open cavity. They proved that in low Richardson numbers, the streamlines are not drawn into the cavity, and in the high Richardson numbers, the streamlines are inclined inward and contain vortices. Wong and Saeid [26] studied the mixed convection around the cooling jet inside the open cavity. They found that Nu_{ave} increased with increasing Péclet number and decreasing the depth of the cavity. Abu-Nada and Chamkha [27] studied the mixed convection of a nanofluid in an inclined cavity, numerically. Their cavity was square-shaped, and its upper and lower walls were exposed to hot and cold temperatures, respectively. They used water-alumina nanofluid. They found that the heat transfer coefficient increased significantly in the presence of nanoparticles. Mahmoudi et al. [28] conducted a numerical study of free convection in an open cavity with two hot sources attached to horizontal walls. They concluded that the streamlines and the isotherm lines were highly dependent on Rayleigh numbers and the distance between the hot sources. In a study of the combined effect of Joule heating and hydrodynamic magnetism, Rahman et al. [29] showed that as the aspect ratio increases, the Nusselt number decreases, the Sherwood increases, and the temperature function remains almost constant. Barnoon et al. [30] studied mixed convection heat transfer of a nanofluid in a porous enclosure. In their work, the enclosure was equipped with rotating circular cylinders and filled. They examined the heat transfer using LTE and LTNE models. They found that the use of rotating cylinders could play an amazing role in improving heat transfer. The same author investigated the effect of heat transfer on the destruction of the gland in biological tissue [31]. Using intense heating, it was shown that tissue can be easily destroyed. Mahmoodi [32] studied the free convection of water-copper nanofluids with a finite volume method in an "L-shaped" cavity. He found that in all aspect ratios, the average Nusselt number improves with increasing Rayleigh number and volume fraction of nanoparticles. Mahmoudi et al. [33] examined the effect of a baffle movement on the convective heat transfer in a channel with heating components. The increase in baffle height at different Richardson numbers is not so great. Parvin and Nasrin [34], similar to Mojumder et al. [35] examined a cavity containing a hot cylindrical piece. They showed that increasing the Reynolds number caused the Nusselt number to increase. Sebdani et al. [36] investigated the mixed convection of water-alumina nanofluid in a square cavity. The left and right walls of the cavity were exposed to cold temperatures and had a constant velocity. The other walls were insulated and only part of the lower wall was exposed to hot temperature. They concluded that as the heat source moves toward the sidewall, the heat transfer rate also increases. Parvin et al. [37] studied the impacts of Soret and Dufour coefficients on natural convection flow phenomena in a partially heated square cavity saturated with water-alumina nanofluid. The upper and lower walls of the cavity were exposed to hot and cold temperatures, respectively, and the other walls were insulated. They found that that both heat and mass transfer were increased by Soret and Dufour coefficients. Sheikhzadeh et al. [38] investigated the free convection in a square cavity with a central heat source. They found that in the studied geometries, as the Rayleigh number increased, the boundary layer became thinner and the heat transfer improved. Mansour et al. [39] investigated the free convection of fluid flow and heat transfer in a "T-shaped" cavity containing a water-Copper nanofluid numerically. The results showed that Nu_{ave} increased with increasing Rayleigh number and ϕ. Abbasian et al. [40]

examined free convection in a sloping "L-shaped" cavity containing a water-copper nanofluid. Their results showed that a decrease in the shape factor and an increase in ϕ led to an increase in Nu_{ave}. Sheikholeslami et al. [41] investigated the free convection of a nanofluid in a cavity. The results showed that Nu_{ave} decreased with increasing the Buoyancy force. Bakier [42] studied the numerical free convection in an open C-shaped cavity containing nanofluid along with a hot source on the cavity wall and found that the density of streamlines and isotherm lines at the top of the cavity was higher. Nasrin and Alim [43] talked about free convection in a closed cavity filled with nanofluids. Their results show that the size of the largest and smallest vortices between the horizontal wall and the hot obstacle did not differ much. Esfe et al. [44] studied the mixed convection in a cavity containing a water-alumina nanofluid with a hot internal source. They found that Nu_{ave} for all ϕ increases with decreasing Richardson number. Further studies on heat transfer within T-shaped cavities in Refs. [52–54] are recommended. In Ref. [52–54], there was only one T-shaped cavity (without thermal barrier) to which a magnetic field was applied and a single-phase nanofluid flowed through it. However, the effect of the magnetic field was considered as a negative factor. Fluid flow and nanofluid heat transfer in cavities using new mechanisms are introduced as valuable numerical studies [55–60]. Also, These mechanisms can be merged with other nanostructures in Refs. [49–51].

A review of the literature shows strong studies on the heat transfer of nanofluids within cavities. However, heat transfer in the T-shaped cavity has received less attention. This study investigates fluid flow and heat transfer in a T-shaped cavity using a thermal barrier. The thermal barrier is placed in different places inside the cavity to achieve the best heat transfer rate. Different aspect ratios are investigated to achieve the best heat transfer rate using a two-phase model.

2. Problem statement and governing equations

2.1. Definition of the problem

The geometry studied in this study is a T-shaped lid-driven cavity and a thermal barrier. The studied cavity is examined in different aspect ratios of AR = 0.2, 0.3, and 0.4, as well as the different positions of the thermal barrier in the cavity. The lid of the cavity moves from left to right at the velocity of V_{lid} and is located at a temperature of 300 K. All walls of the cavity, except for the thermal barrier walls, are considered adiabatic, and the thermal barrier walls are at a constant temperature above the cover temperature. The temperature difference between the thermal barrier walls and the cover is determined by Ri = 0.1, 1, and 10. The schematic of the problem is shown in Fig. 1. The driving force in the geometry under study is the high velocity of the lid and the buoyancy force due to the temperature difference between the thermal barrier and the moving lid. This flow is considered to be the incompressible water-alumina nanofluid in $\phi = 0$, 1, 2, and 3 % inside a cavity. The Newtonian base fluid is assumed, and density changes are considered in such a way that the motion factor can be quickly attributed to the moving lid and the density changes. Any heat effect from the pressure field is ignored. Mixed convection in the cavity includes natural convection due to constant temperature wall temperature differences and forced convection due to lid movement.

Also, the information about the present problem is presented in Table 1.

2.2. Mixture two-phase model

Continuity equation [45]:

$$\vec{\nabla}.\left(\rho_m \vec{V}_m\right) = {}^{\circ} \tag{1}$$

Momentum equation [45]:

$$\vec{\nabla}.\left(\rho_m \vec{V}_m \vec{V}_m\right) = -\vec{\nabla}P + \vec{\nabla}.\left[\mu_m\left(\vec{\nabla}\vec{V}_m + \vec{\nabla}\vec{V}_m^{T}\right)\right] + \rho_m \vec{g} + \vec{F} - \vec{V}.\left(\sum_{k=1}^{n}\phi_k\rho_k \vec{V}_{dr,k}\vec{V}_{dr,k}\right) \tag{2}$$

The k subscript represents the number of phases distributed in the base fluid. In this part, k = 1 and the third statement in Equation (2) are defined as follows [45],

$$\vec{\nabla}.\left(\sum_{k=1}^{n}\phi_k\rho_k \vec{V}_{dr,k}\vec{V}_{dr,k}\right) = \vec{\nabla}.\left(\phi_p\rho_p \vec{V}_{dr,p}\vec{V}_{dr,p}\right) \tag{3}$$

Energy equation [28]:

$$\vec{\nabla}.\left(\sum_{k=1}^{n}(\rho_k c_k)\phi_k \vec{V}_k T\right) = \vec{\nabla}.\left(k_{eff}T\right) \tag{4}$$

The equation for the volume ratio of particles is defined as follows:

$$\vec{\nabla}.\left(\phi_p\rho_p \vec{V}_m\right) = -\vec{\nabla}.\left(\phi_p\rho_p \vec{V}_{dr,p}\right) \tag{5}$$

In the equations presented, the parameters are defined as follows:

$$\vec{V}_m = \frac{\sum_{k=1}^{n}\phi_k\rho_k \vec{V}_k}{\rho_{eff}} \tag{6}$$

$$\vec{\tau} = \mu_{eff}\vec{\nabla}V_m \tag{7}$$

In Eq. (3), $\vec{V}_{dr,k}$ is the buoyancy velocity for the second phase is defined as the difference between the nanoparticle velocity and the mixture velocity,

$$\vec{V}_{dr,k} = \vec{V}_k - \vec{V}_m \tag{8}$$

Relative velocity is defined as the difference between the velocity of the second phase (nanoparticles) and the velocity of the first phase (base fluid):

$$\vec{V}_{pf} = \vec{V}_p - \vec{V}_f \tag{9}$$

and

$$\vec{V}_{dr,p} = \vec{V}_{pf} - \sum_{k=1}^{n}\frac{\phi_k\rho_k}{\rho_{eff}}\vec{V}_{fk} \tag{10}$$

In Eq. (10), the drag function is represented as follows [45],

$$\vec{V}_{pf} = \frac{\rho_p d_p^2}{18\mu_f f_{drag}}\frac{\left(\rho_p - \rho_{eff}\right)}{\rho_p}\vec{a} \tag{11}$$

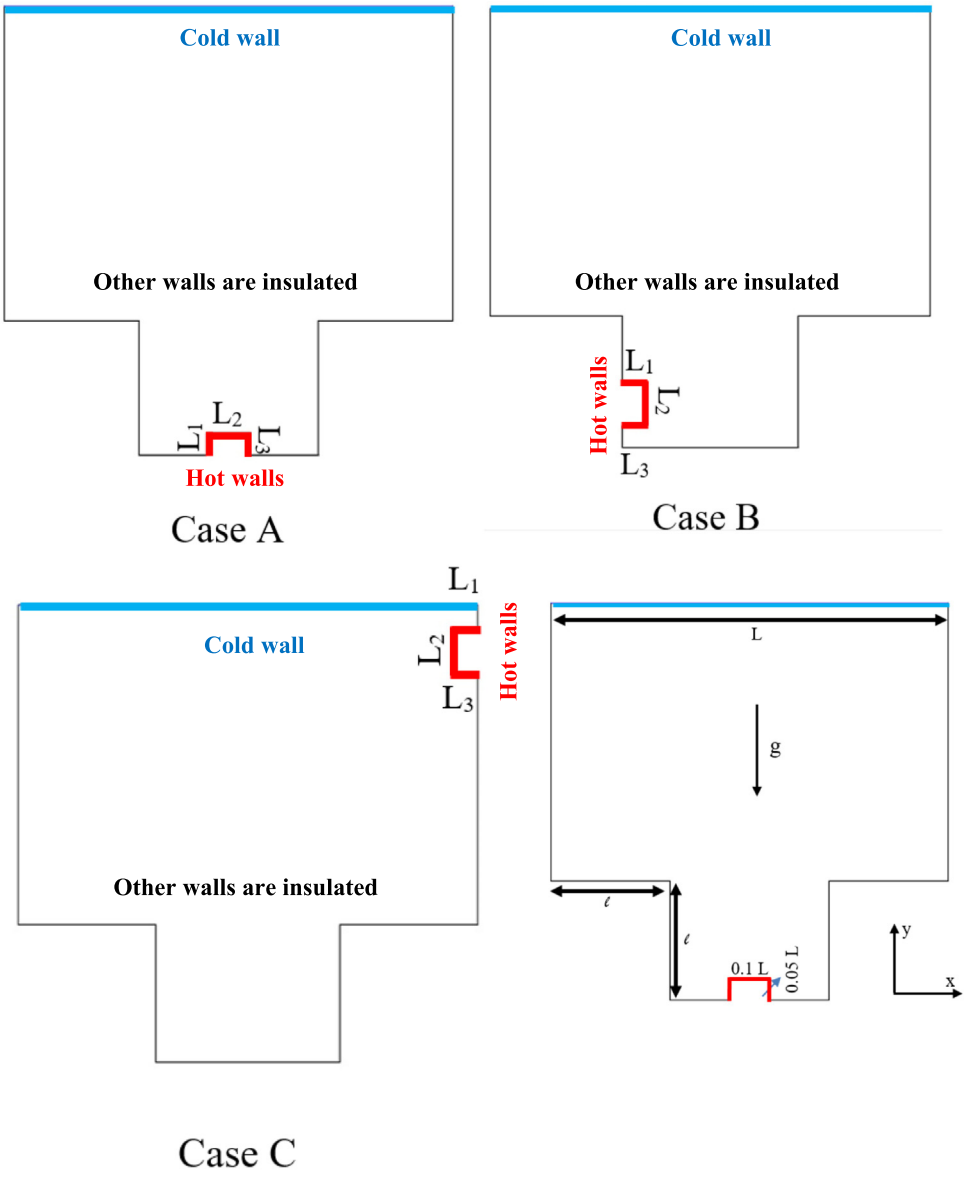

Fig. 1 Schematic of the problem.

Table 1 The information of the present research.

ϕ (%)	Ri	Gr	Re	$\Delta T(K)$	$V_{lid}\,(m/s)$
0	0.1	100	31.622	13.79	0.0221
0	1	100	10	13.79	0.007
0	10	100	3.16	13.79	0.00221
1	0.1	100	31.622	15.915	0.0233
1	1	100	10	15.915	0.00337
1	10	100	3.16	15.915	0.00233
2	0.1	100	31.622	18.797	0.0249
2	1	100	10	18.797	0.00786
2	10	100	3.16	18.797	0.00249
3	0.1	100	31.622	22.725	0.0268
3	1	100	10	22.725	0.00849
3	10	100	3.16	22.725	0.00268

$$f_{drag} = \begin{cases} 1 + 0.15Re_p^{0.687} Re_p \leqslant 1000 \\ 0.15Re_p Re_p > 1000 \end{cases} \quad (12)$$

$\vec{a}$ in Equation (11) is defined as follows [45],

$$\vec{a} = \vec{g} - \left(\vec{V}_m.\vec{\nabla}\right)\vec{V}_m \quad (13)$$

The relationships used to calculate the effective properties of nanofluid are as follows:

Effective density:

$$\rho_{eff} = (1-\phi)\rho_f + \phi\rho_p \quad (14)$$

Effective thermal expansion coefficient [46]

$$\beta_{eff} = \left[\frac{1}{1+\frac{(1-\phi)\rho_f}{\phi\rho_p}}\frac{\beta_p}{\beta_f} + \frac{1}{1+\frac{\phi}{(1-\phi)}\frac{\rho_p}{\rho_f}}\right].\beta_f \quad (15)$$

Effective *viscosity* [47],

$$\mu_{eff} = \frac{\mu_f}{(1-\phi)^{0.25}} \quad (16)$$

Effective thermal conductivity [46],

$$\frac{k_{eff}}{k_f} = \frac{k_p + 2k_f - 2\phi(k_f - k_p)}{k_p + 2k_f + \phi(k_f - k_p)} \quad (17)$$

The properties calculated for the nanofluid are also given in Table 2.

The local Nusselt number along the hot wall can be obtained by the following formula:

$$Nu_{loc} = \frac{\frac{\partial T}{\partial n}L}{T_h - T_c} \quad (18)$$

The average Nusselt number along the cavity is calculated as follows:

$$Nu_{ave} = \frac{1}{L*}\int_0^{L*} Nu_{loc}(dL*) \quad (20)$$

Richardson, Grashof, and Reynolds numbers for nanofluids are defined as follows:

$$Ri = \frac{Gr}{Re^2}, \quad Gr = \frac{\rho_{eff}^2 g\beta_{eff}\Delta T L^3}{\mu_{eff}^2}, \quad Re = \frac{\rho_{eff}V_{lid}L}{\mu_{eff}} \quad (21)$$

The dimensionless length of the thermal barrier, aspect ratio, and other dimensionless numbers of the problem are also given below,

$$L_1 + L_2 + L_3 = L* \quad (22)$$

$$\frac{Lenght}{L*} = L**$$

$$AR = l/L$$

Table 2 Thermophysical properties of base fluid (water) and nanoparticles (alumina) [61].

	$\rho\left(\frac{kg}{m^3}\right)$	$Cp\left(\frac{J}{kgK}\right)$	$k\left(\frac{W}{mK}\right)$	$\mu\left(\frac{kg}{ms}\right)$
water	993	4178	0.628	0.000695
Al_2O_3	3880	733	36	–

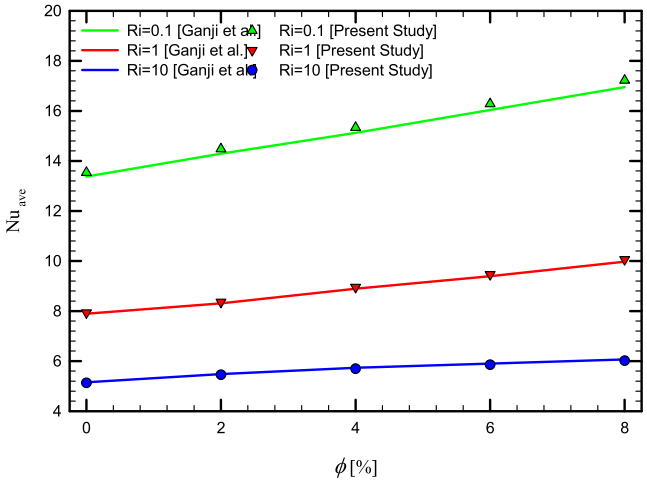

Fig. 2 Validation diagram.

$$\Delta T = T_h - T_c$$

$$Y* = \frac{y}{L}$$

$$X* = \frac{x}{L}$$

2.3. Methods and boundary conditions

In this research, for simulation, the steady two-dimensional method was studied with double-precision. The solver type in this study is pressure-based, which has been used to link the velocity and pressure. Also, for discrete equations, the second-order UPWIND method is used. A convergence criterion in this paper for all residues is 10^{-6} for all equations [32–34]. The boundary conditions used in this study are:

- The constant temperature on thermal barrier walls
- A constant temperature of 300 K on the lid
- Fixed velocity corresponding to Richardson number for the lid

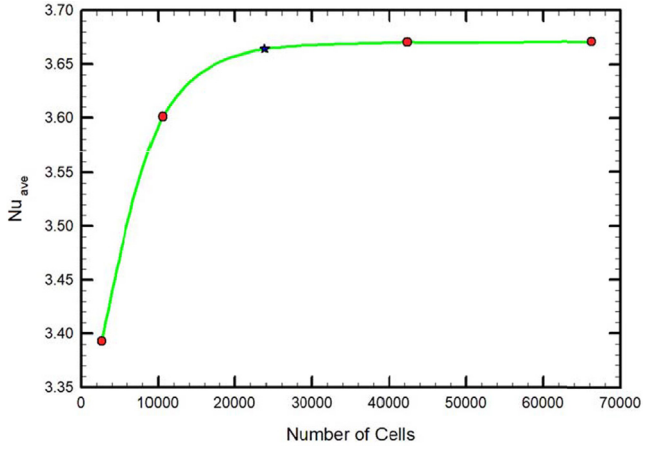

Fig. 3 The Nu_{ave} versus the number of computational grids in Ri = 0.1, ϕ = 3%, and AR = 0.2 for case.

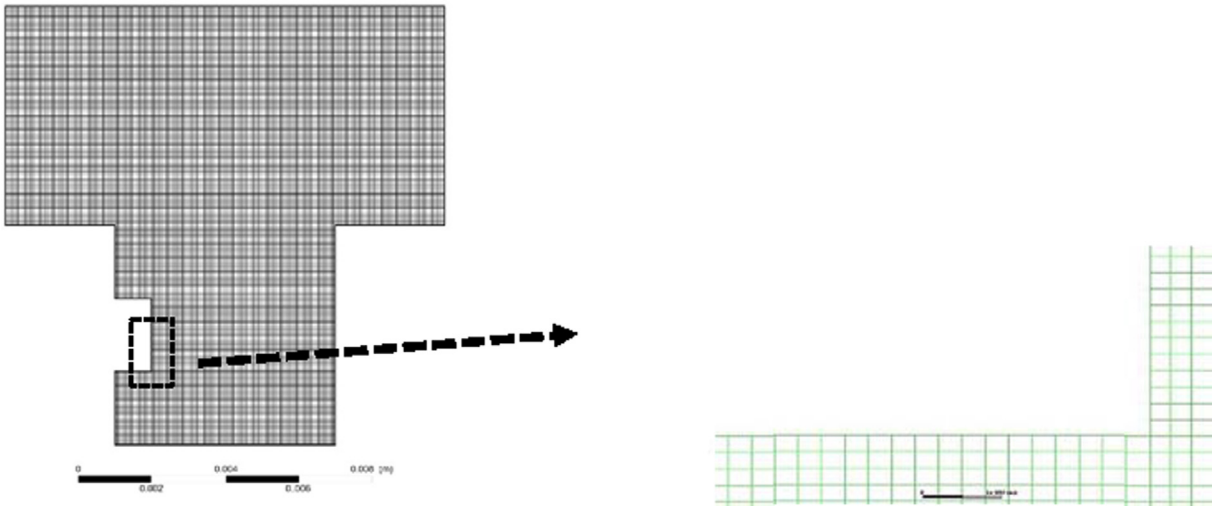

Fig. 4 An example of the computational grid used in this study.

- Other walls are considered adiabatic.
- The gravitational acceleration is equal to 9.81 m /s^{2,} and the working pressure is equal to 1 atm.
- Properties are independent of temperature and are only a function of ϕ.
- The Boussinesq approximation has been used to investigate the effect of temperature on fluid density difference.

$$coldwall V_m = V_{m,x}, T = T_c \tag{23}$$

$$\text{hot}wall V_{m,x} = V_{m,y} = 0, T = T_h$$

$$otherwalls V_{m,x} = V_{m,y} = 0, \frac{\partial T}{\partial x} = \frac{\partial T}{\partial y} = 0$$

2.4. Validation, grid computing, and grid independency

To ensure the accuracy of the results of the present study simulation, the method used in this study is compared with Alinia et al. [48]. They investigated the mixed convection of a nanofluid in a square cavity in the Richardson number range is 0.01 < Ri < 100 using a two-phase mixture method. Because the range of Richardson numbers in the present study is 0.1 < Ri < 10, the results were compared in Ri = 0.1, 1, and 10. As can be seen in Fig. 2, the results are well overlapped. The difference in results in most cases is < 1.5%. Given that the error below 3% is generally acceptable for comparison with numerical tasks, these results are quite acceptable.

This study uses a uniformly structured computational grid. Also, to grid independency, the Nu_{ave} in Ri = 0.1, ϕ = 3%, and the case a in AR = 0.2 have been investigated. Therefore, to investigate and compare this parameter, the results of five computational grids have been compared and shown in Fig. 3. Fig. 3 shows the graph of the Nu_{ave} versus the number of computational grids in Ri = 0.1, ϕ = 3 %, and AR = 0.2 for case a. As can be seen from step 3, Nu_{ave} changes from very small to very small, so that the error rate drops below 3 %. As a result, 250,000 cells will be used in the research, and the computational grid will be optimal. An example of the computational grid used in this study is also shown in Fig. 4.

3. Results and discussion

3.1. Effect of Richardson number on hydrodynamic and thermal parameters

3.1.1. The local Nusselt number

Fig. 5 shows a diagram of Nu_{loc} versus dimensionless length in Ri = 0.1, 1 and 10, AR = 0.2, 0.3 and 0.4, and cases a, b, and c in ϕ = 1 %. The Nu_{loc} is calculated on the thermal barrier. Since the three sides of the thermal barrier are related to the fluid, it can be seen that in all diagrams, the Nu_{loc} graph is divided into three sections with three different behaviors. Each section corresponds to one side of the barrier. Based on the figures, it can be seen that in all cases, as the Richardson number increases, the overall level of the Nu_{loc} decreases, so that the highest Nusselt number is related to the Ri = 0.1 and the lowest is related to Ri = 10. The reason for this can be better understood by considering the Richardson number formula. As Richardson number increases, the velocity of the lid decreases, and as a result, the intensity of the secondary flow created also decreases. In other words, with the increase in Richardson number, the rate of forced convection decreases, and the share of natural convection increases.

3.1.2. Average Nusselt number

Fig. 6 shows the Nu_{ave} versus Richardson number in AR = 0.2, 0.3 and 0.4, ϕ = 0, 1, 2 and 3%, the geometric cases a, b and c, and Ri = 0.1, 1 and 10. As can be seen, the relationship between the Nu_{ave} and the Richardson number is reversed, so that with the increase in Richardson numbers, the Nu_{ave} decreases. The reason is the decrease in the share of heat transfer of forced convection and the dominance of free convection over forced convection. For case a, and AR = 0.2, the rate of decrease in the Nu_{ave} in Ri = 1 and 10 compared to the Ri = 0.1 in ϕ = 0% is 36.34 and 79.98%, respectively. The rate of these reductions in ϕ = 1% was 34.12% and 80.47%, respectively; in ϕ = 2% equal to 33.85 and 80.93% and in

$\phi = 3\%$ equal to 33. 38 and 81.19 %. It can also be seen that the highest Nu_{ave} is related to Ri = 0.1 and $\phi = 3\%$, which is equal to 4.87 and the lowest Nu_{ave} is related to Ri = 10, which is equal to 2.58. For case a and AR = 0.3, the rates of decrease in the Nu_{ave} in Ri = 1 and 10 compared to Ri = 0.1 in $\phi = 0\%$ are 22.3 and 50.27%, respectively. The values of these reductions in $\phi = 1\%$ are equal to 22.06 and 50.52%, in $\phi = 2\%$ are equal to 21.69 and 50.66% and in $\phi = 3\%$ are equal to 21.34 and 50.87%. It can also be seen that the highest Nu_{ave} is related to Ri = 0.1, and $\phi = 3\%$, which is equal to 3.18, and the lowest Nu_{ave} is related to Ri = 10, and $\phi = 0\%$ which is equal to 2.05. For geometric case a and AR = 0.4, the rates of decrease in the Nu_{ave} in Ri = 1 and 10 compared to the Ri = 0.1 in $\phi = 0\%$ are 10.5 and 22.33%, respectively. Decrease in these values in $\phi = 1\%$ equal to 10.37 and 22.46%, in $\phi = 2\%$ equal to 10.19 and 22.56% and in $\phi = 3\%$ equal to 9.94 and 22.62%. It can also be seen that the highest Nu_{ave} is related to Ri = 0.1 and $\phi = 3\%$ which is equal to 1.45 and the lowest Nu_{ave} is related to the Ri = 10 number and $\phi = 0\%$ which is equal to 1.17. For the geometric case b and the AR = 0.2, the rates of decrease in the Nu_{ave} in Ri = 1 and 10 compared to the Ri = 0.1 in $\phi = 0\%$ are equal to 3.87 and 70.96%, respectively. The values of these reductions in the $\phi = 1\%$ are equal to 30.66 and 71.32%, in the $\phi = 2\%$ are equal to 30.43 and 71.63% and in the $\phi = 3\%$ are equal to 30.01 and 71.76 %. It can also be seen that the highest Nu_{ave} is related to Ri = 0.1, and $\phi = 3\%$, which is equal to 4.36, and the lowest Nu_{ave} is related to Ri = 10, and $\phi = 0\%$, which is equal to 2.44. For case b and AR = 0.3, the rates of decrease in the Nu_{ave} in Ri = 1 and 10 compared to the Ri = 0.1 and $\phi = 0\%$ are equal to 22.3% and 50.2%, respectively. The values of these reductions in $\phi = 1\%$ are equal to 22.06% and 50.47%. In $\phi = 2\%$ these reductions are equal to 21.79% and 50.71% and in $\phi = 3\%$ these reductions are equal to 21.4% and 50.8%. It can also be seen that the highest Nu_{ave} is related to Ri = 0.1 and $\phi = 3\%$, which is equal to 3.19, and the lowest Nu_{ave} is related to Ri = 10, and $\phi = 0\%$ which is equal to 2.06. For case b and AR = 0.4, the decrease in the Nu_{ave} in Ri = 1 and 10 compared to the Ri = 0.1 in $\phi = 0\%$ is 12.32% and 26.23%, respectively. The values of these reductions in $\phi = 1\%$ are equal to 12.17% and 26.38%, in $\phi = 2\%$ equal to 11.97% and 26.52% and in $\phi = 3\%$ are equal to 11.69% and 26.61 %. It can also be seen that the highest Nu_{ave} is related to Ri = 0.1 and $\phi = 3\%$, which is equal to 1.72. The lowest Nu_{ave} is related to Ri = 10, and $\phi = 0\%$ which is equal to 1.34. For case c and AR = 0.2, the rates of decrease in Nu_{ave} in Ri = 1 and 10 compared to the Ri = 0.1 in $\phi = 0\%$ are equal to 19.03% and 30.65%, respectively. The values of these reductions in $\phi = 1\%$ are equal to 18.03% and 28.18%, and in $\phi = 2\%$ these reductions are equal to 18.69% and 29.51% and in $\phi = 3\%$ these reductions are equal to 19.38% and 31.04%. It can also be seen that the highest Nu_{ave} is related to Ri = 0.1 and $\phi = 3\%$, which is equal to 11.87, and the lowest Nu_{ave} is related to Ri = 10 which is equal to 9.05. For case c and AR = 0.3, the rates of decrease in the Nu_{ave} in Ri = 1 and 10 compared to the Ri = 0.1 in $\phi = 0\%$ are equal to 17.74% and 27.28%, respectively. The values of these reductions in $\phi = 1\%$ are equal to 18.25 and 28.32%. Average Nusselt number in the case c is far higher than the case b and a because of lid-driven and thermal barrier in close vicinity. Moreover, in case c, when AR grows, Average Nusselt reduces more slowly as Ri number intensifies from Ri = 1 to Ri = 10

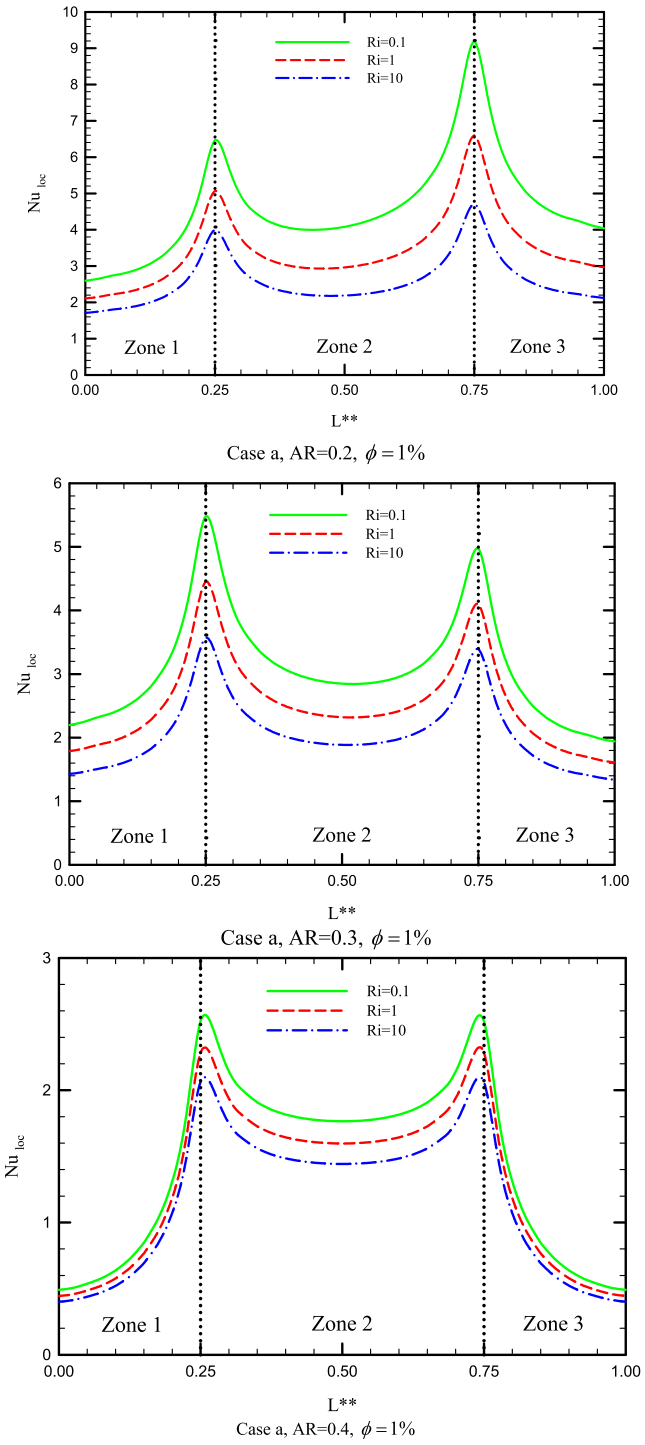

Fig. 5 Nu_{loc} versus dimensionless length.

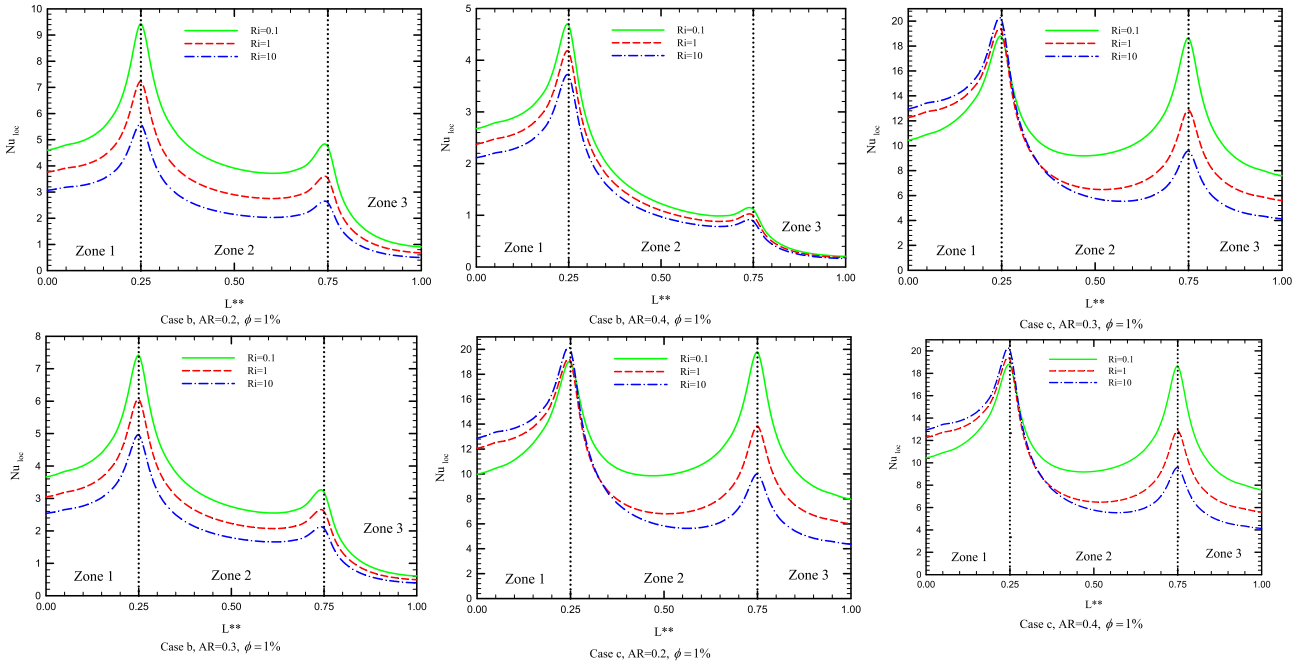

Fig. 5 (*continued*)

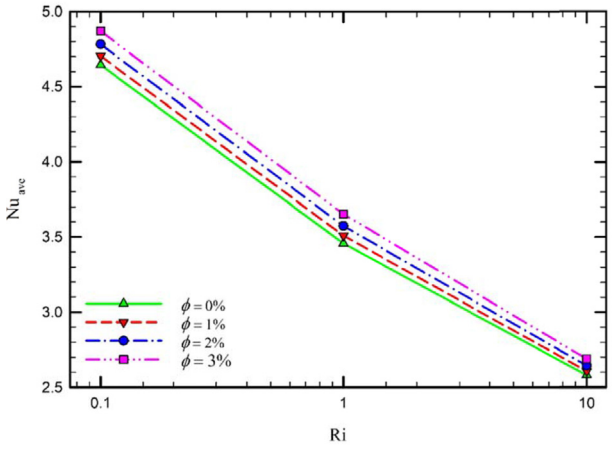

Fig. 6 Nu_{ave} versus Richardson number at a different.

than Ri intensifies from Ri = 0.1 to Ri = 0.1. This is because of thermal barrier position, which is close to the top of the cavity. As the volume fraction increases due to the increased thermal conductivity of the nanofluid, the heat transfer increases in all cases.

3.1.3. Temperature and velocity contours

Fig. 7 shows the temperature distribution contour in case a and AR = 2.0, ϕ = 0%, and Ri = 0.1, 1, and 10. As can be seen, the density of the isotherm lines near the thermal barrier is higher in lower Richardson numbers. The higher density of the isotherm lines near the thermal barrier indicates a higher temperature gradient. A higher temperature gradient is also one of the signs of a higher heat transfer rate, which can be

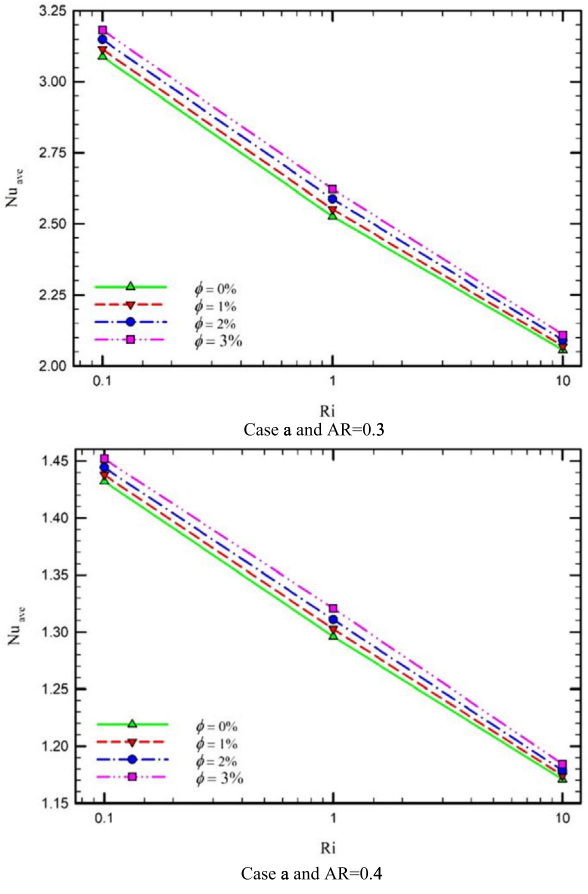

Fig. 6 (*continued*)

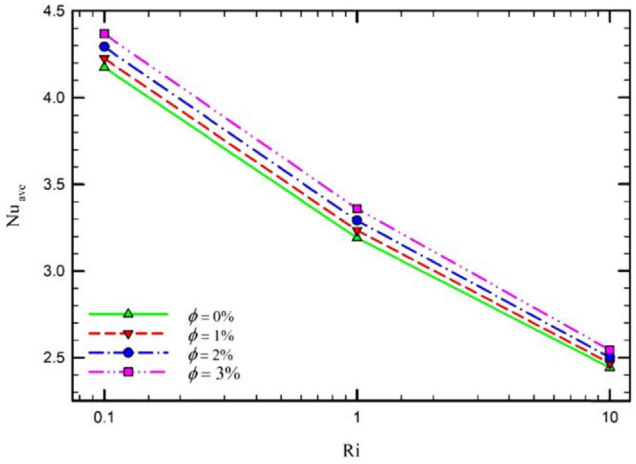

Case b and AR=0.2

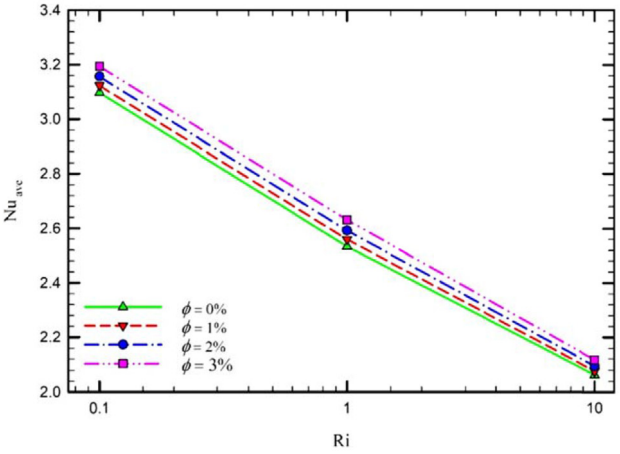

Case b and AR=0.3

Fig. 6 (*continued*)

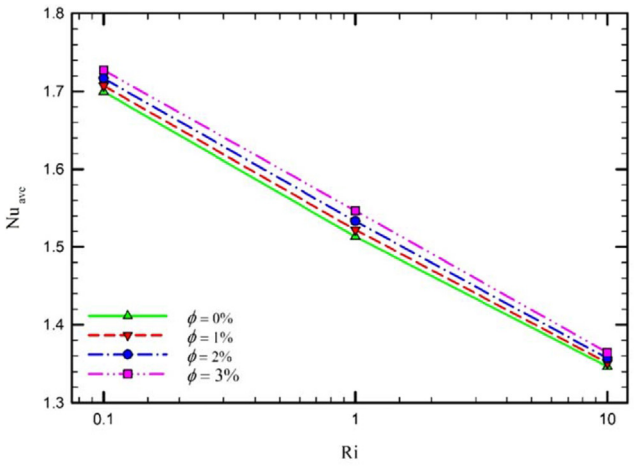

Case b and AR=0.4

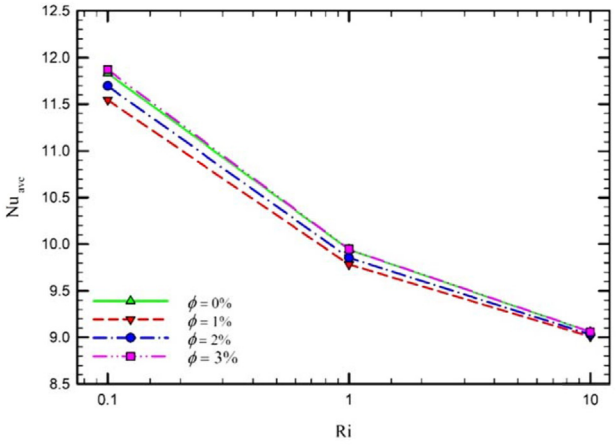

Case c and AR=0.2

Fig. 6 (*continued*)

seen in the lower Richardson numbers. It can also be seen that as the Richardson number increases, the isotherm lines become more uniform (horizontally). The reason for this can be described by the fact that with the increase in the Richardson number, the share of heat transfer of forced convection decreases, and the share of heat transfer of free convection increases.

Figs. 8 and 9, respectively, show the velocity distribution contour and velocity vector in geometric case a, AR = 0.4, $\phi = 0\%$, and Ri = 0.1, 1, and 10. As can be seen, the line density in the velocity contour is inversely related to Richardson number so that as Richardson number increases, the line density decreases. The main density of lines in all cases is near the moving lid. As Richardson number increases, the velocity of the moving lid decreases, so the density of the lines, which also indicates the velocity gradient, also decreases. Also, according to Fig. 9, which shows the velocity vector, it can be seen that as the Richardson number increases, the order of magnitude of the velocity vectors decreases at all points. Also, the velocity vectors near the moving lid are more significant than other points.

Figs. 10 and 11 show the streamlines and vorticity contours for case a, in $\phi = 0\%$, AR = 0.2, and Ri = 0.1, 1, and 10. Due to the streamlines, it can be seen that the density of the streamlines on the sides of the cavity is higher than the center of the cavity, which indicates more velocity in the parts where the density of the streamlines is higher. The highest density of streamlines is also near the driving lid.

3.1.4. Velocity profile

Fig. 12 shows the velocity profile in the y-direction in the center of the cavity in geometric cases a, b, and c, Ri = 0.1, 1, and 10, $\phi = 1\%$, and AR = 0.2, 0.3, and 0.4. As can be seen, the velocity profile behavior in all cases has a prominent feature, so that by moving from the highest amount of Y* to its lowest level, first the velocity is in its maximum state and then rapidly decreases to 0. This behavior occurs in the range of $0.75 < Y^* < 1$. Then, as the amount of Y* decreases, the value of the velocity increases again, but in the negative direction, and by reaching another maximum value, it decreases again and tends to zero, which is the same point $Y^* = 0$. Therefore, it can be concluded that the behavior of the velocity profile is divided into two main parts (in AR = 0.2). The first part is approximately $0 < Y^* < 0.75$, and the second part is approximately $0.75 < Y^* < 1$. The reason for this can be attributed to fluid circulation in the first part. In the second part, the movement of the moving lid has affected the fluid layers around it.

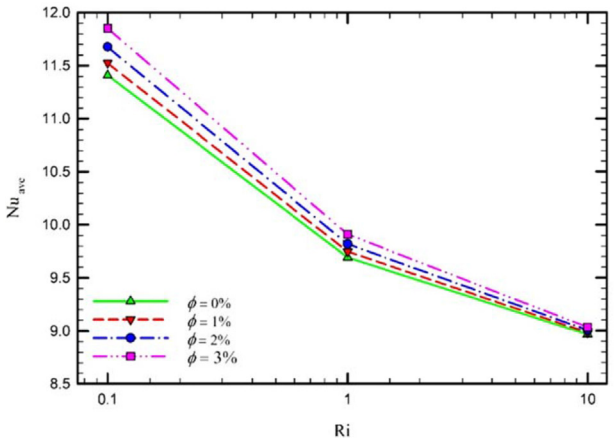

Case c and AR=0.3

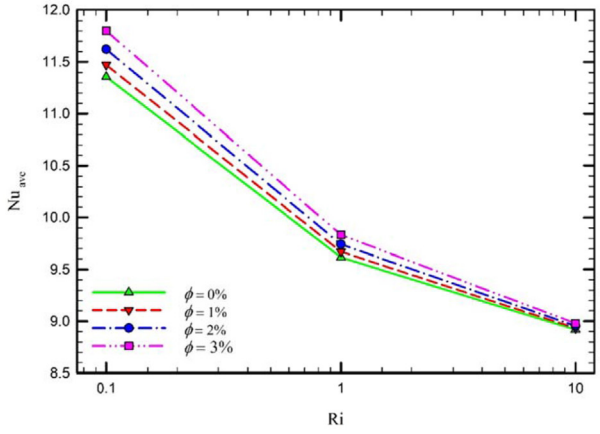

Case c and AR=0.4

Fig. 6 (*continued*)

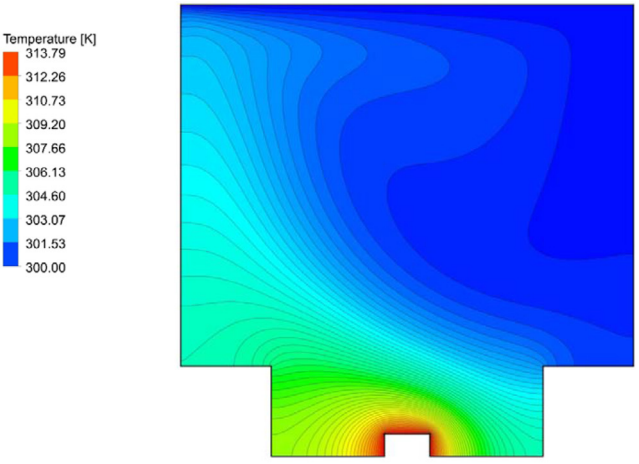

Ri=0.1

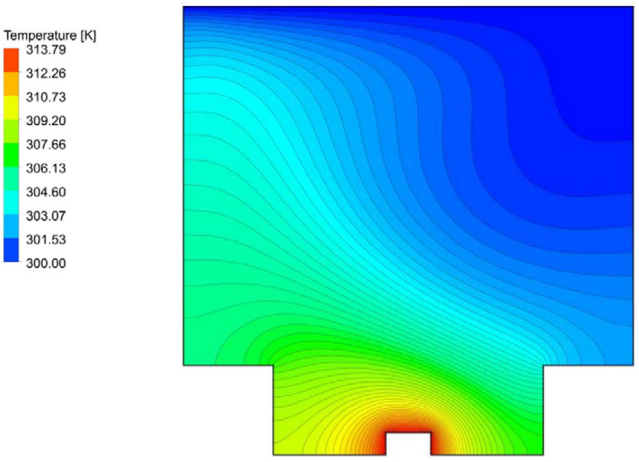

Ri=1

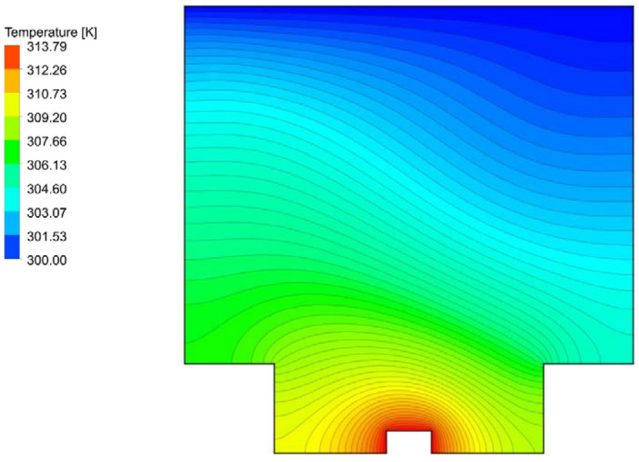

Ri=10

Fig. 7 Isotherm contours in case a and $\phi = 0\%$, AR = 0.2.

Another point that can be mentioned is the slope of the velocity profile chart; so that, with the increase of Richardson number, the velocity profile becomes flatter, which can be attributed to the decrease in lid's velocity, which also leads to a reduction in circulation. Therefore, with the increase in the Richardson number, the amount of velocity in both areas decreases.

3.2. Investigating the effect of aspect ratio

3.2.1. Check the velocity and temperature contours

Fig. 13 shows the velocity contour in case a, Ri = 0.1, $\phi = 0\%$, and AR = 0.2, 0.3, and 0.4. As can be seen, by increasing the aspect ratio, the density of the streamlines distances from the thermal barrier. In other words, in smaller aspect ratios, the line's density is also higher near the thermal barrier, and this density decreases with increasing aspect ratio. Since one of the factors in increasing heat transfer is the increase in velocity gradient on the thermal barrier walls and by considering that the higher density of velocity lines indicates a higher velocity gradient, so we can see the reduction of velocity gradient on the thermal by an increase in the aspect ratio.

Figs. 14 and 15, respectively, show the stream and vorticity lines for case a in $\phi = 0\%$, Ri = 0.1 and AR = 0.2, 0.3 and 0.4, respectively. As can be seen, unlike Richardson number's changes, which had little effect on the stream line's behavior, the changes in the aspect ratio had a significant effect on the streamlines; so that, as the aspect ratio increased, the circulating area became smaller and eventually at AR = 0.4, another circulating area is created in the lower space of the cavity, which has a very low velocity. Also, by increasing the aspect

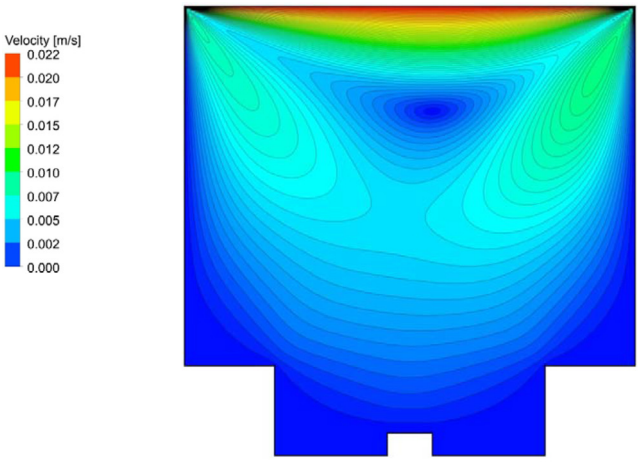

Ri=0.1

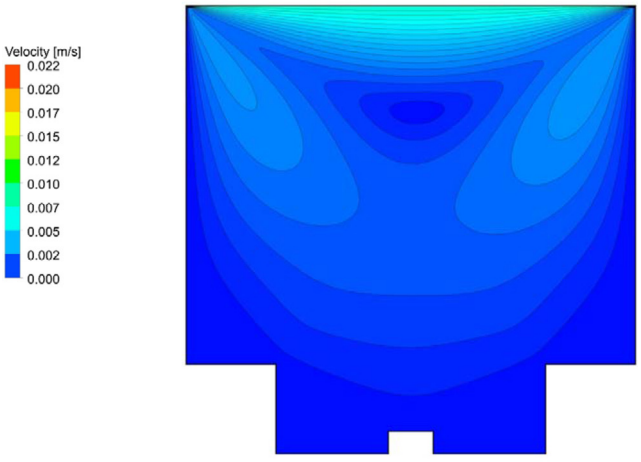

Ri=1

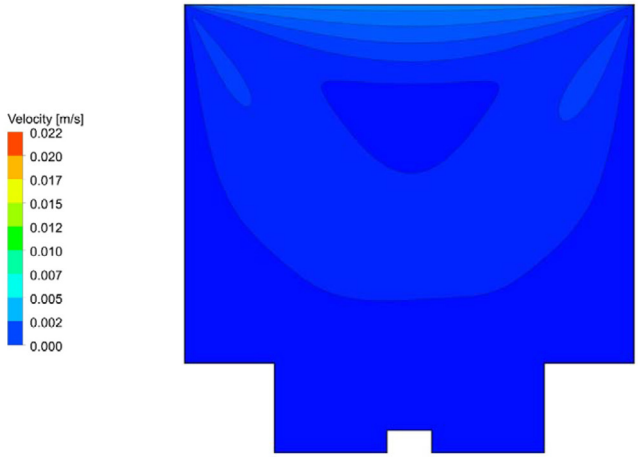

Ri=10

Fig. 8 Cantour of velocity distribution in case a and $\phi = 0\%$, AR = 0.2.

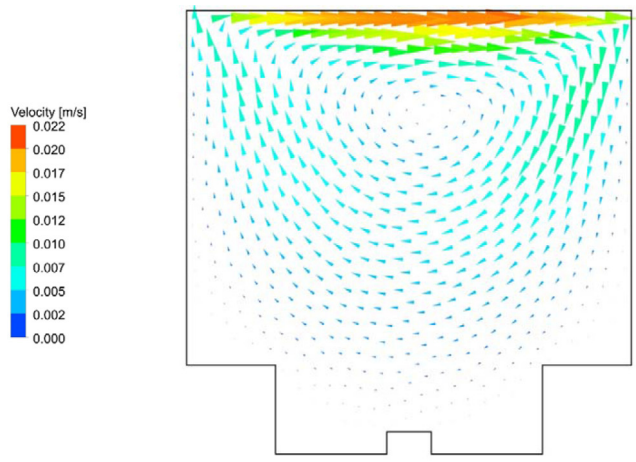

Ri=0.1

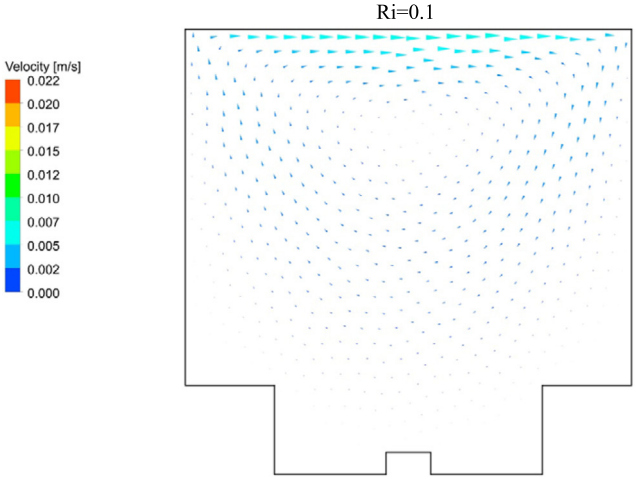

Ri=1

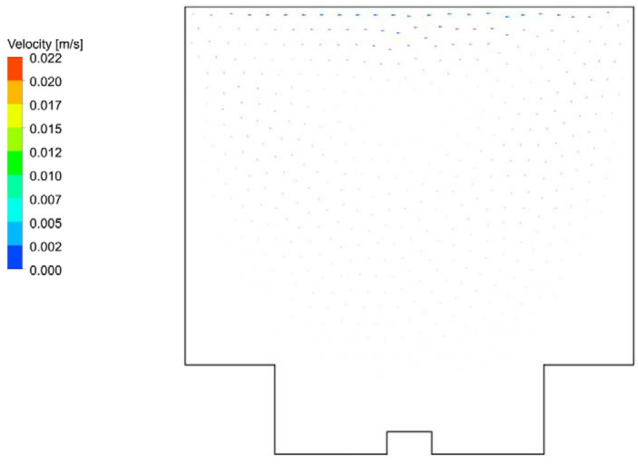

Ri=10

Fig. 9 Velocity vectors in case a and $\phi = 0\%$, AR = 0.2 and different Richardson numbers.

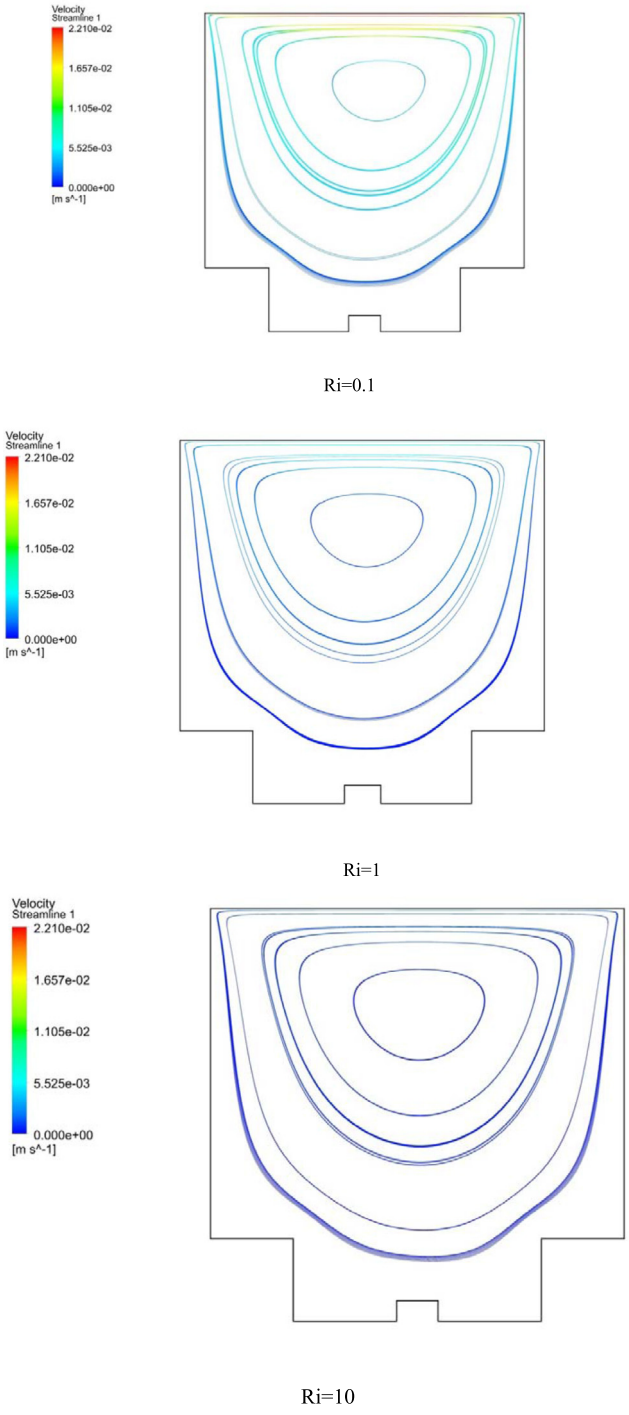

Fig. 10 Contour of streamlines in case a and $\phi = 0\%$, AR = 0.2.

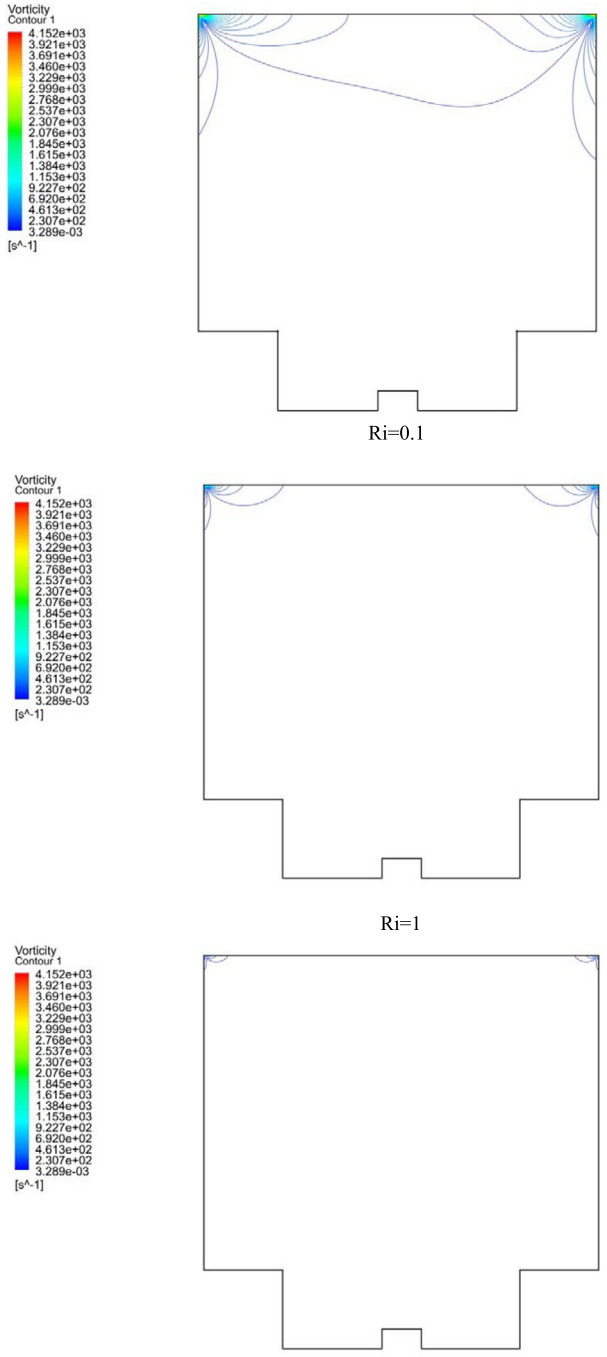

Fig. 11 Vorticity contour for case a and $\phi = 0\%$, AR = 2.0.

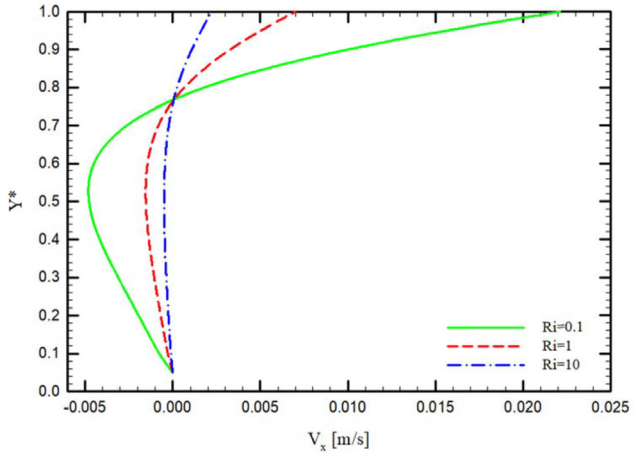

Case a and AR=0.2

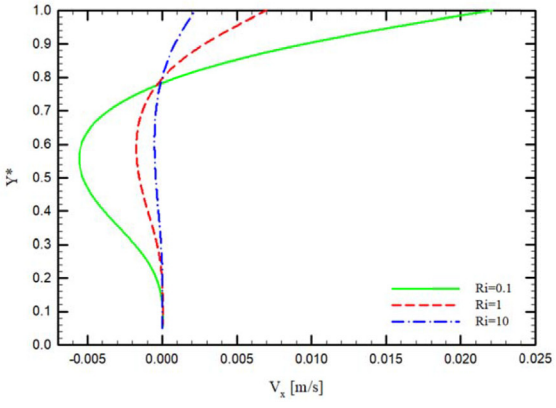

Case a and AR=0.3

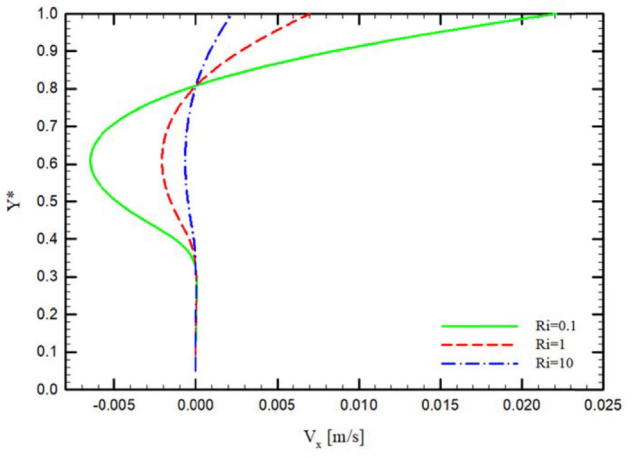

Case a and AR=0.4

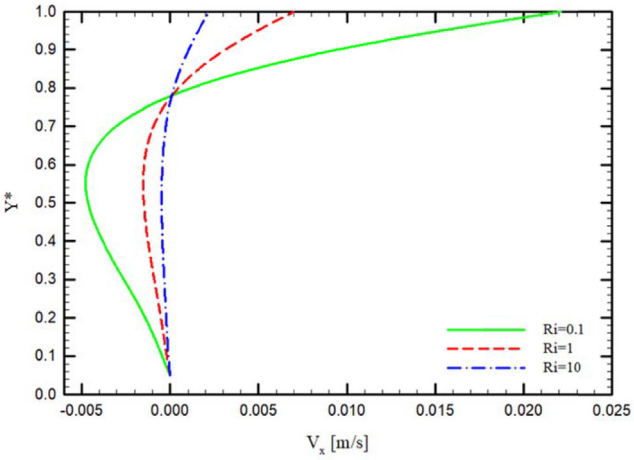

Case b and AR=0.2

Fig. 12 Velocity profile along the y-axis in x = L /2 for $\phi = 1\%$.

Fig. 12 (*continued*)

ratio, the circulation area is directed towards the upper wall of the cavity and also stretches along the x-axis.

Fig. 16 shows the contour of the isotherm lines in case a, $\phi = 0\%$, Ri = 0.1 and AR = 0.2, 0.3, and 0.4. As can be seen, as the aspect ratio increases, the density of the isotherm lines decreases near the thermal barrier, indicating a decrease in temperature gradient and a decrease in heat transfer. The reason for this can be described as the fact that by increasing the aspect ratio, does not only the circulation in the vicinity of the thermal barrier decrease, but also the fluid range around the thermal barrier decreases. This reduction causes the surrounding fluid to lose its heat-cooling potential.

3.2.2. Local Nusselt number

Fig. 17 shows a diagram of the local Nusselt number in terms of dimensionless length L** for geometric cases a, b and c, AR = 0.2, 0.3, and 0.4, in $\phi = 1\%$ and Ri = 0. 1. As can be seen, in geometric cases a and b, as the aspect ratio increases, the overall level of the local Nusselt number chart on all sides of the thermal barrier decreases, but this is not the case in case c, and the Nusselt number increases in some areas with increasing aspect ratio and reduced in others. As explained, the reason for this is related to the distance of the thermal barrier to the lid as well as the more limited circulation area.

Fig. 18 shows the Nu_{ave} versus AR in Ri = 0.1, 1, and 10, $\phi = 0$, 1, 2, and 3 %, for the geometric case a. As can be seen, in case a, increasing the aspect ratio in all Richardson numbers and ϕ leads to a decrease in the Nu_{ave}. In all cases, the highest Nu_{ave} is related to the lowest Richardson number and the lowest aspect ratio, and the highest Nu_{ave} is related to the highest Richardson number and the highest aspect ratio. In $\phi = 0\%$, the values of the Nu_{ave} in Ri = 0.1 and in AR = 0.2, 0.3,

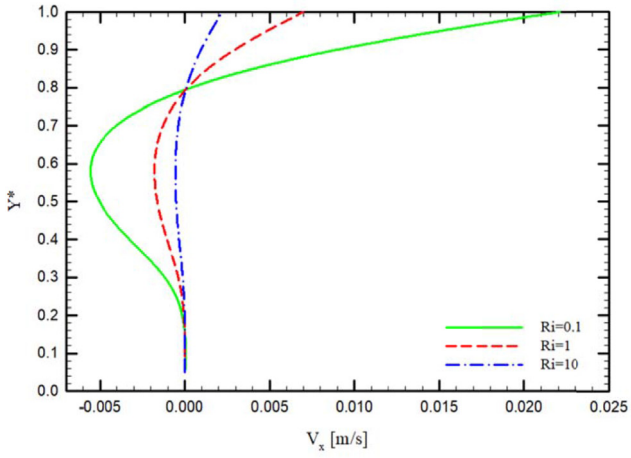

Case b and AR=0.3

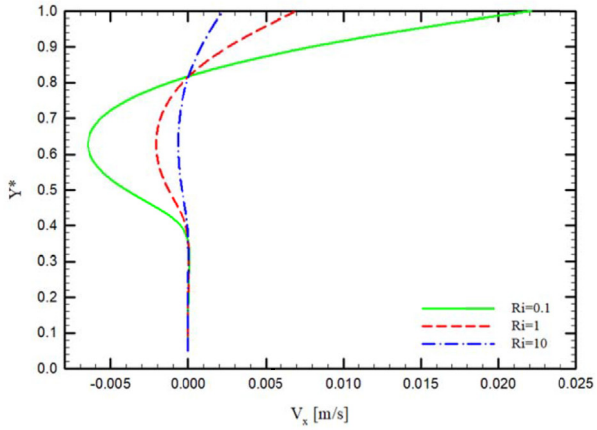

Case b and AR=0.4

Fig. 12 (*continued*)

and 0.4, respectively, equal to 4.64, 3.08 and 1.43. These values for Ri = 1 are equal to 3.45, 2.52, and 1.29 and in Ri = 10 are equal to 2.58, 2.05, and 1.17. The rate of decrease in the Nu_{ave} in AR = 0.3 and AR = 0.4 compared to the AR = 0.2 in Ri = 0.1 is equal to 50.33 and 224.25 %, respectively. The values of these reductions in Ri = 1 are equal to 36.84 and 166.68 %, and in Ri = 10 are equal to 25.51 and 120.41 %. In ϕ = 1%, the values of the Nu_{ave} in the Ri = 0.1 in AR 0.2, 0.3 and 0.4, respectively, equal to 4.7, 3.11, and 1.43. The values of these reductions in Ri = 1 are equal to 3.5, 2.55, and 1.3 %, and in Ri = 10 are equal to 2.6, 2.06, and 1.17 %. The rate of decrease in the Nu_{ave} in AR = 0.3 and 0.4 compared to AR = 0.2 in Ri = 0.1 is equal to 51.06 and 227.21%, respectively. The values of these reductions in Ri = 1 are equal to 37.48 and 169.28%, and in Ri = 10 are equal to 25.99 and

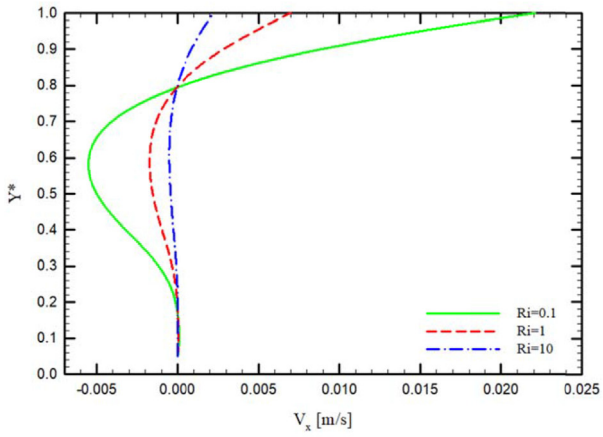

Case c and AR=0.2

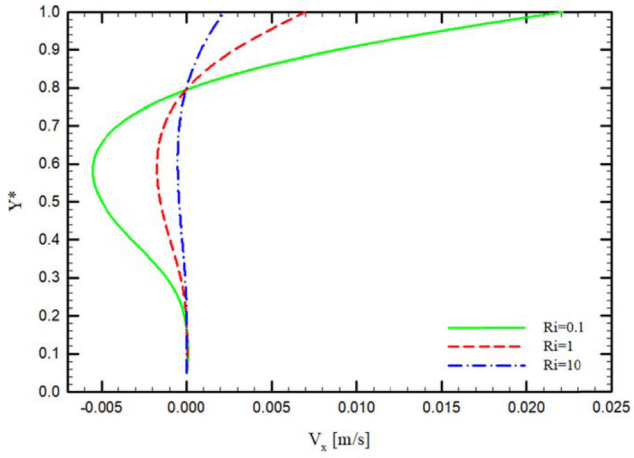

Case c and AR=0.3

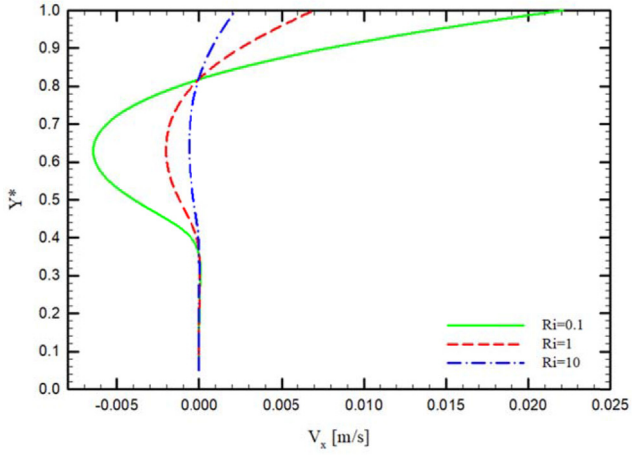

Case c and AR=0.4

Fig. 12 (*continued*)

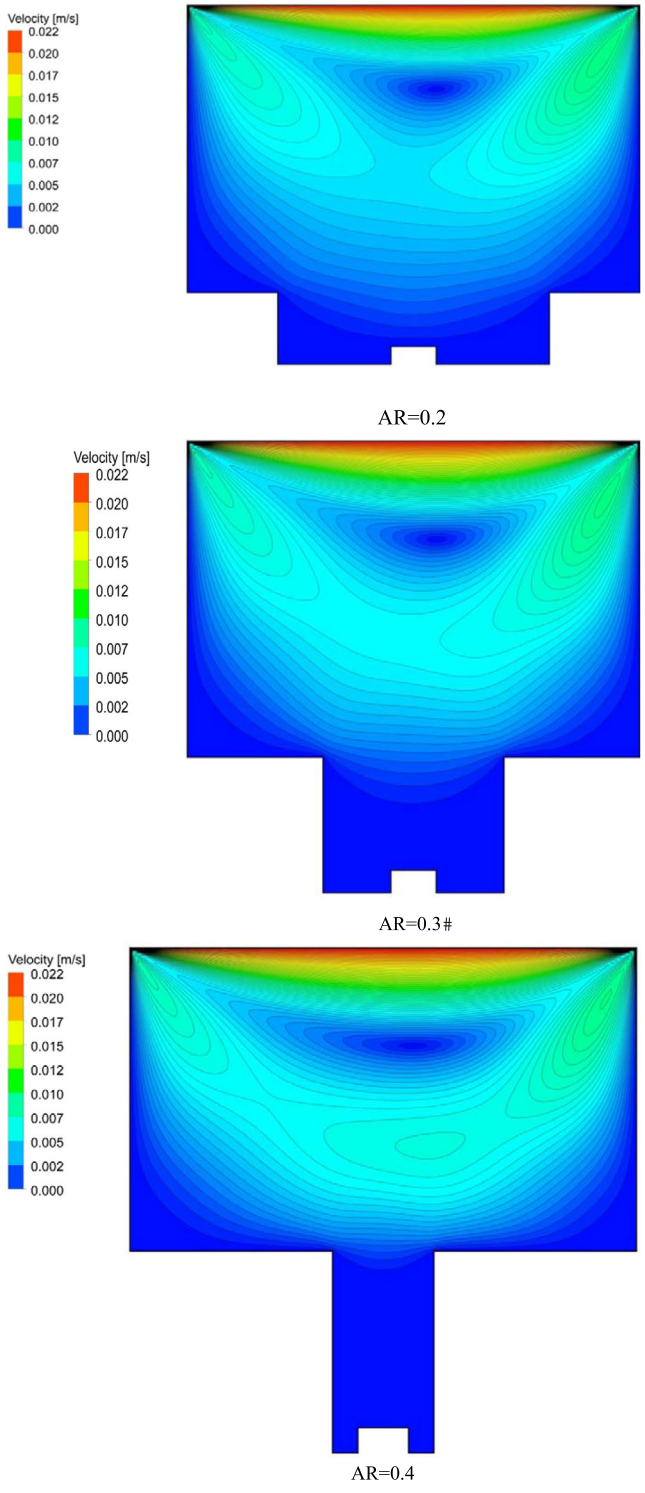

Fig. 13 Velocity contours in case a, Ri = 0.1, $\phi = 0\%$.

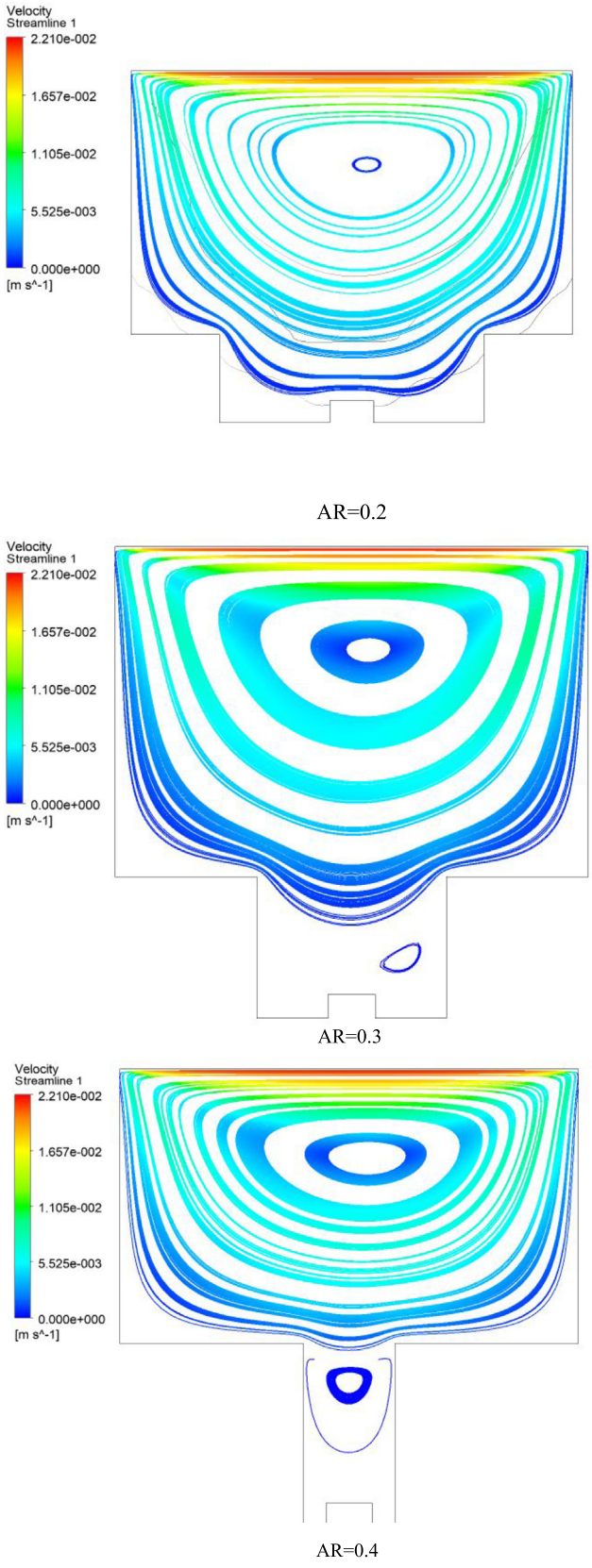

Fig. 14 Streamline contours in case a, Ri = 0.1, $\phi = 0\%$.

122.04%. In $\phi = 2\%$, the values of the Nu_{ave} in Ri = 0.1 in AR = 0.2, 0.3 and 0.4, respectively, equal to 4.78, 3.14 and 1.44. The values of these reductions in Ri = 1 are equal to 3.57, 2.58 and 1.31 and in Ri = 10 are equal to 2.64, 2.09 and 1.17. The rate of decrease in the Nu_{ave} in AR = 0.3 and 0.4 compared to the AR = 0.2 in Ri = 0.1 is equal to 51.88

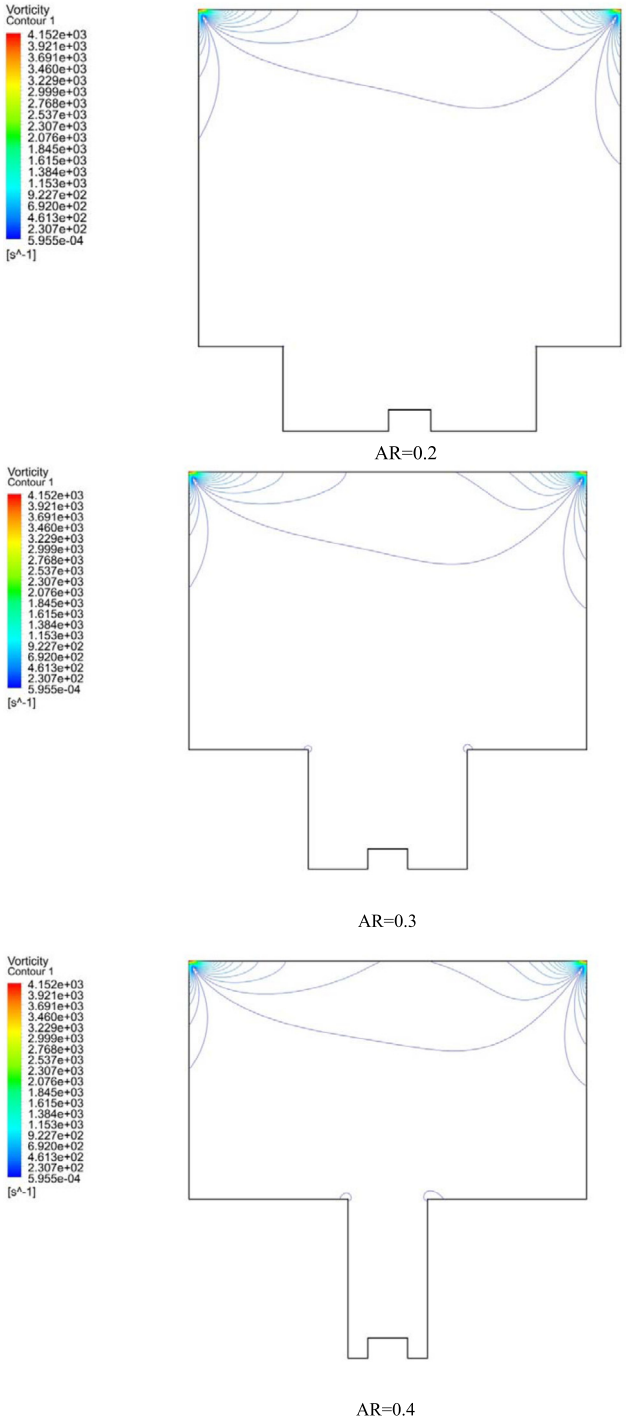

Fig. 15 Vorticity contour in case a, Ri = 0.1, $\phi = 0\%$.

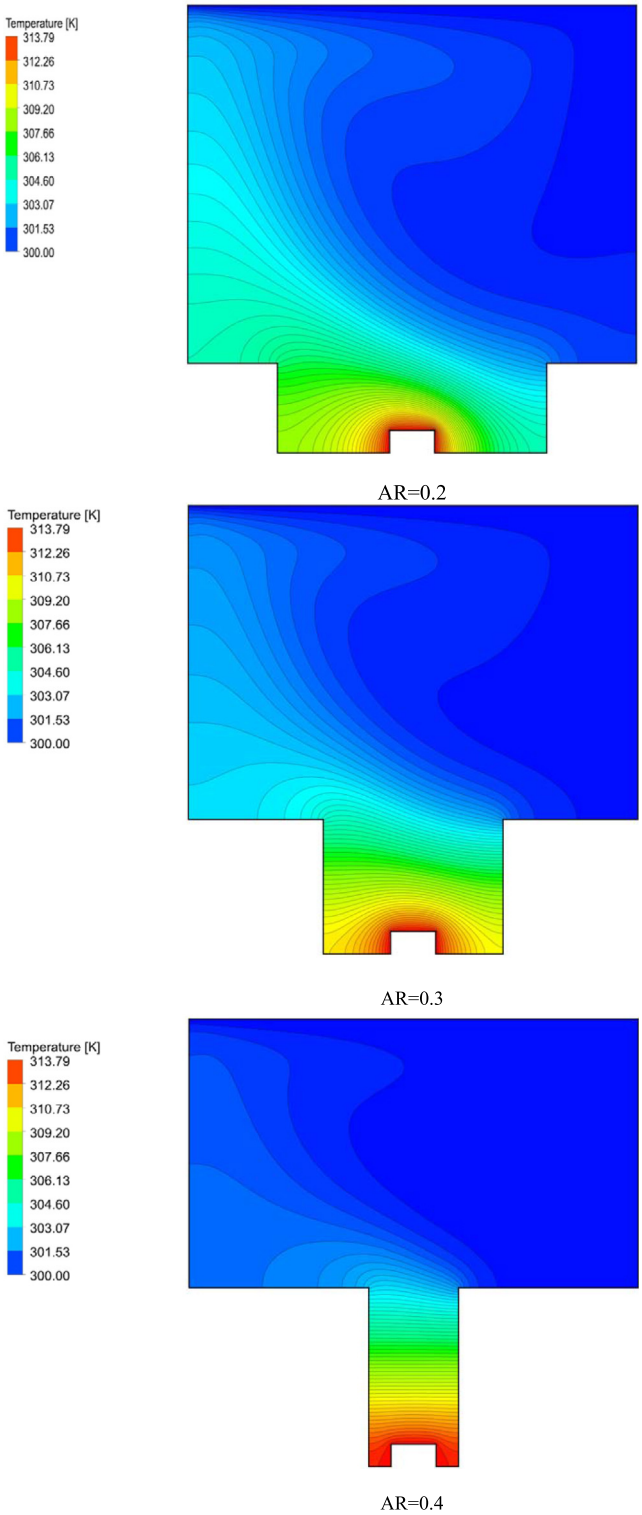

Fig. 16 Contour of isotherm lines in case a, Ri = 0.1, $\phi = 0\%$.

and 231.1%, respectively. These values in Ri = 1 are equal to 38.08 and 172.56 and in Ri = 10 are equal to 26.47 and 124.28 %. In $\phi = 3\%$, the values of Nu_{ave} in Ri = 0.1 and AR = 0.2, 0.3, and 0.4, respectively, equal to 4.87, 3.18 and 1.45, respectively. The values of these reductions in Ri = 1 are equal to 3.65, 2.62, and 1.32 and in Ri = 10 are equal to 2.68, 2.1, and 1.18. The rate of decrease in the Nu_{ave} in AR = 0.3 and 0.4 compared to the AR = 0.2 in Ri = 0.1 is equal to 53.07 and 235.46%, respectively. These values in Ri = 1 are equal to 39.24 and 176.5 and in Ri = 10 are 27.45 and 127.02%.

Fig. 19 shows the Nu_{ave} versus aspect ratio in Ri = 0.1, 1 and 10, for the geometric case b in $\phi = 0$, 1, 2 and 3%. In $\phi = 0\%$, the amount of Nu_{ave} in Ri = 0.1 and AR = 0.2, 0.3 and 0.4, respectively, equal to 4.17, 3.09 and 1.69. These

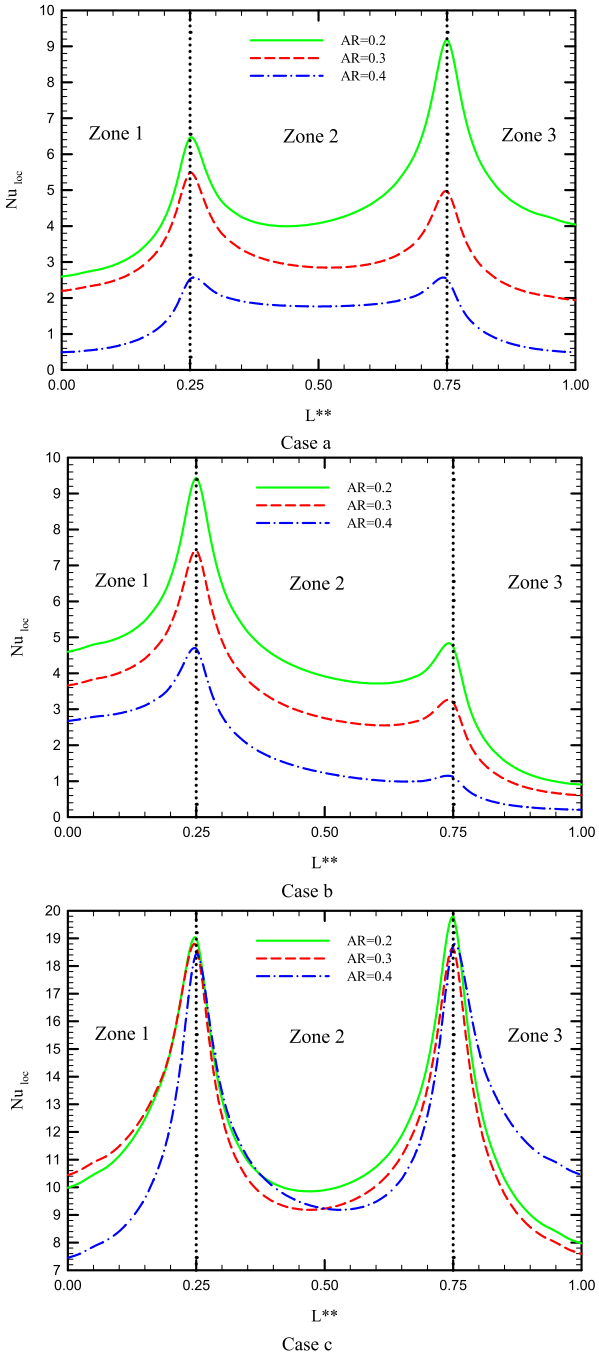

Fig. 17 The local Nusselt number versus dimensionless length in Ri = 0.1 and $\phi = 1\%$.

values in Ri = 1 are 3.19, 2.53 and 1.51 and in Ri = 10 are 2.44, 2.06, and 1.34. The rate of decrease in the Nu_{ave} in AR = 0.3 and 0.4 compared to AR = 0.2 in Ri = 0.1 is equal to 25.8 and 59.29%, respectively. These values in Ri = 1 are equal to 20.6 and 52.57 and in Ri = 10 are equal to 15.55 and 44.87%. In $\phi = 1\%$, the amount of Nu_{ave} in Ri = 0.1 and AR = 0.2, 0.3 and 0.4 is equal to 4.22, 3.12 and 1.7, respectively. These values in Ri = 1 are equal to 3.23, 2.55 and 1.52 in Ri = 10 are equal to 2.46, 2.07 and 1.35. The rate of decrease in Nu_{ave} in AR = 0.3 and 0.4 compared to AR = 0.2 in Ri = 0.1 is 26.09 and 59.6%, respectively. These values in Ri = 1 are equal to 20.89 and 52.94 and in Ri = 10 are equal to 15.85 and 45.24%. In $\phi = 2\%$, the amount of Nu_{ave} in Ri = 0.1 in AR = 0.2, 0.3 and 0.4 is equal to 4.29, 3.15 and 1.71, respectively. These values in Ri = 1 are equal to 3.29, 2.59 and 1.53 and in Ri = 10 are equal to 2.5, 0.2, and 1.35. The rate of decrease in Nu_{ave} in AR = 0.3 and 0.4 compared to AR = 0.2 in Ri = 0.1 is equal to 26.46 and 60%, respectively. These values in Ri = 1 are equal to 21.25 and 53.41 and in Ri = 10 are equal to 16.26 and 45.74%. In $\phi = 3\%$, the amount of Nu_{ave} in Ri = 0.1 and A = 0.2, 0.3 and 0.4 is equal to 4.36, 3.19 and 1.72, respectively. These values in Ri = 1 are equal to 3.35, 2.63 and 1.54 and in Ri = 10 are equal to 2.54, 2.11 and 1.36. The rate of decrease in the Nusselt number in AR = 0.3 and 0.4 compared to the AR = 0.2 in Ri = 0.1 is equal to 26.88 and 60.45%, respectively. These values in Ri = 1 are equal to 21.68 and 53.96 and in Ri = 10 are equal to 16.75 and 46.35 %

Fig. 20 shows the Nu_{ave} versus AR in Ri = 0.1, 1, and 10, for case c in $\phi = 0$, 1, 2, and 3 %. In $\phi = 0\%$, the amount of Nu_{ave} in Ri = 0.1, in AR = 0.2, 0.3 and 0.4 is equal to 11.83, 11.41, and 11.35, respectively. These values in Ri = 1 are equal to 9.94, 9.69 and 9.61, and in Ri = 10 are equal to 9.05, 8.96 and 8.91. The rate of decrease in the Nu_{ave} in AR = 0.3 and 0.4 compared to AR = 0.2 in Ri = 0.1 is equal to 3.57% and 4.04%, respectively. These values in Ri = 1 are equal to 2.51 and 3.28 and in Ri = 10 are equal to 1.02 and 1.55%. In $\phi = 1\%$, the amount of Nu_{ave} in Ri = 0.1 and AR = 0.2, 0.3 and 0.4 is equal to 11.54, 11.52 and 11.47, respectively. These values in Ri = 1 are equal to 9.78, 9.74 and 9.66 and in Ri = 10 are 9, 8.98 and 8.93. The rate of decrease in the Nu_{ave} in AR = 0.3 and 0.4 compared to AR = 0.2 is 0.17% and 0.65%, respectively. These values in Ri = 1 are equal to 0.36 and 1.15% and in Ri = 10 are equal to 0.28% and 0.84 %. In $\phi = 2\%$, the rate of local Nusselt number in Ri = 0.1 in AR = 0.2, 0.3, and 0.4 is equal to 11.69, 11.67, and 11.62, respectively. These values in Ri = 1 are equal to 9.85, 9.81 and 9.74 and in Ri = 10 are equal to 9.03, 9 and 8.95. The rate of decrease in the Nu_{ave} in the AR = 0.3 and 0.4 compared to AR = 0.2 and Ri = 0.1 is equal to 0.17, 0.62%, respectively. These values in Ri = 1 are equal to 0.36 and 1.14% and in Ri = 10 are 0.3 and 0.8 %. In $\phi = 3\%$, the amount of Nu_{ave} in Ri = 0.1 and AR = 0.2, 0.3 and 0.4, respectively, equal to 111.87, 11.85

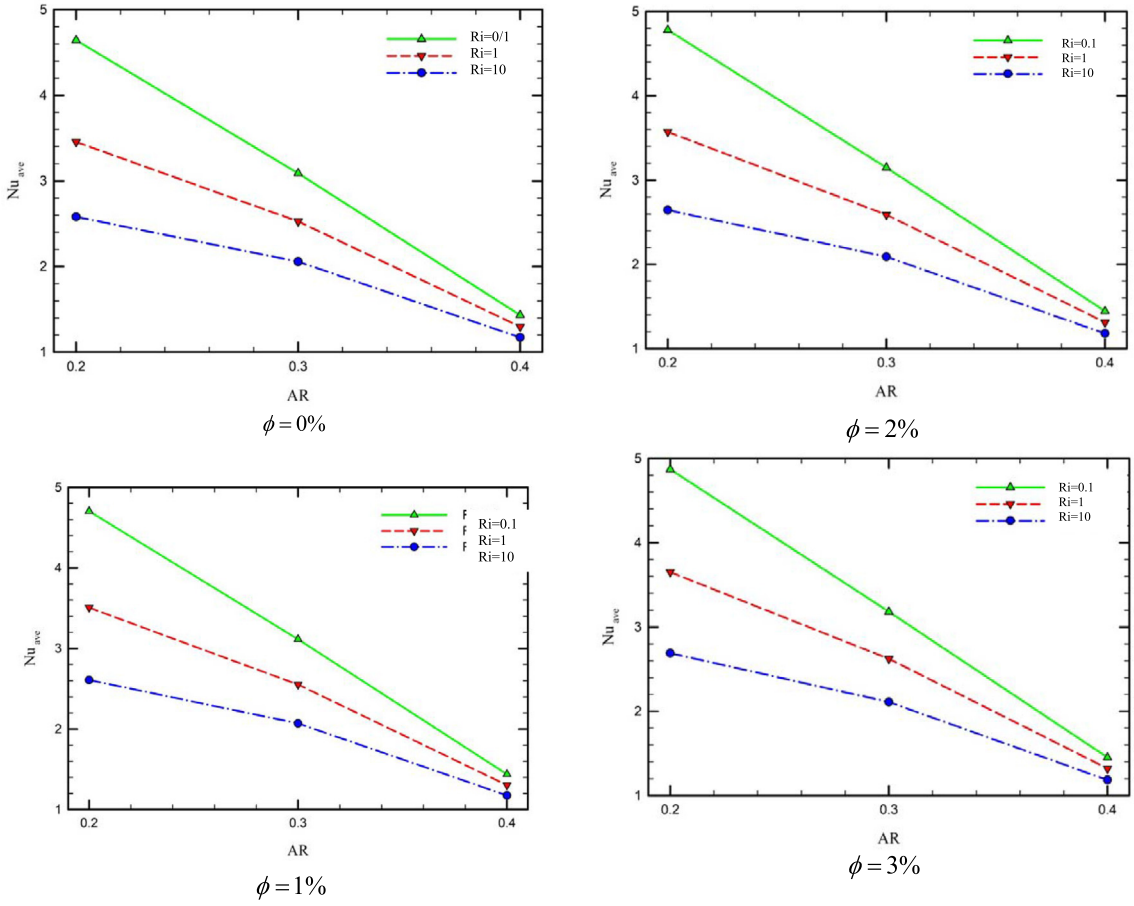

Fig. 18 Nu_{ave} versus AR in case a.

and 11.8. These values in Ri = 1 are equal to 9.94, 9.9 and 9.83, and in Ri = 10 are equal to 9.05, 9.03 and 8.97. The rate of decrease in the Nu_{ave} in AR = 0.3 and 0.4 compared to AR = 0.2 and Ri = 0.16 and 0.6%, respectively. These values in Ri = 1 are equal to 0.35 and 1.13 and in Ri = 10 are 0.31 and 0.9 %.

4. Conclusion

In this study, the numerical simulation of mixed convection of water-aluminum oxide nanofluid in a T-shaped lid-driven cavity was investigated in the presence of a thermal barrier located in different positions of the cavity using the two-phase mixture method. This study included Ri = 0.1, 1 and 10, ϕ = 0, 1, 2 and 3 %, AR = AR = 0.2, 0.3 and 0.4. Also, three different positions for the thermal barrier were checked.

- Increasing the Richardson number reduces the heat transfer rate due to the reduction of secondary flows through the moving lid.
- Increasing the ϕ increases in heat transfer.
- Increasing the aspect ratio of the cavity reduces the heat transfer.
- The reduction in heat transfer rate is greater due to the increase in the aspect ratio of the abacus in cases a and b than in case c because the circulation caused by the secondary flow created by the lid in the vicinity of the thermal barrier is more limited.
- Case c has a higher heat transfer than in cases a and b, which can be attributed to the fact that it is adjacent to the driving lid.

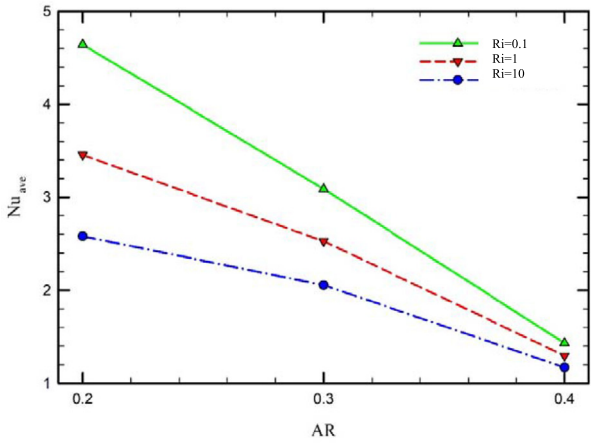

$\phi = 0\%$

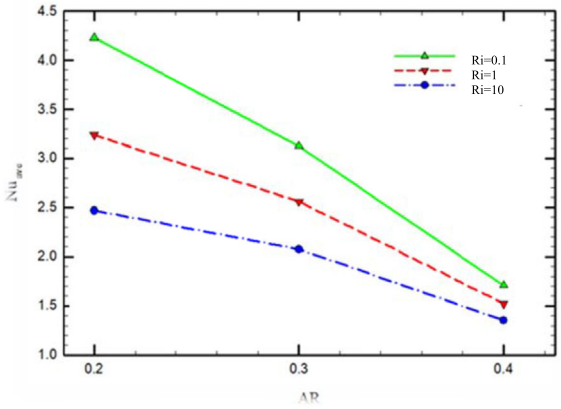

$\phi = 1\%$

Fig. 19 Nu_{ave} versus AR in case b.

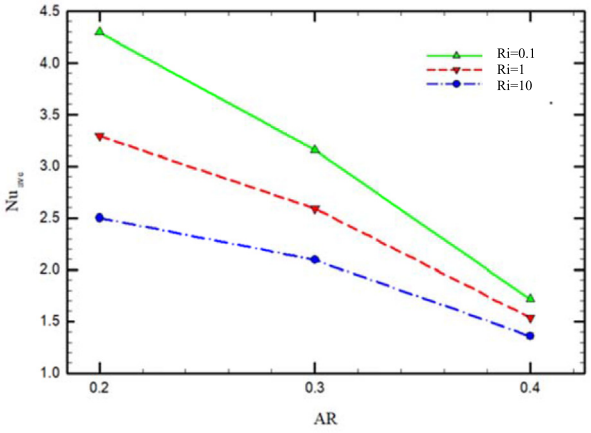

$\phi = 2\%$

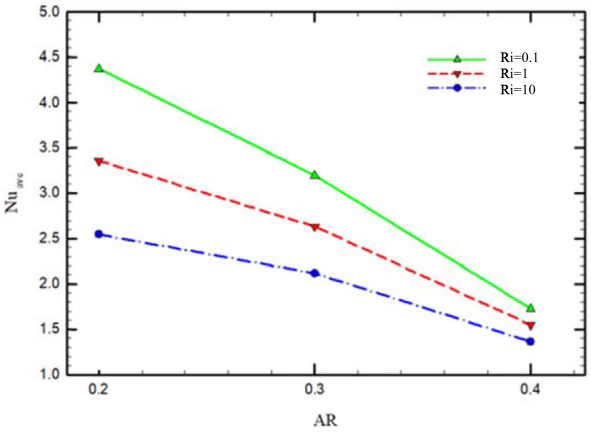

$\phi = 3\%$

Fig. 19 (*continued*)

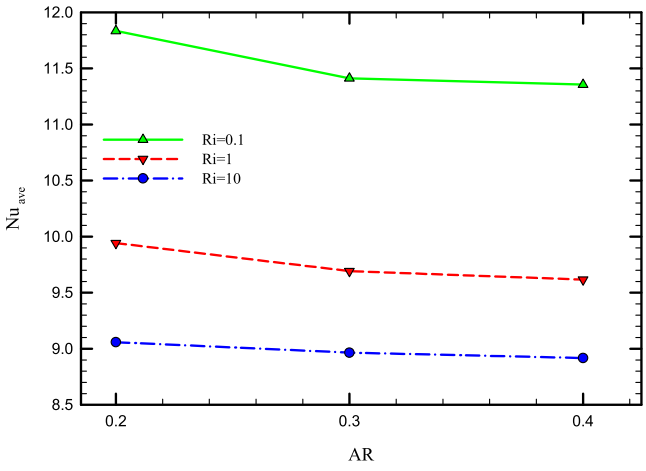

$\phi = 0\%$

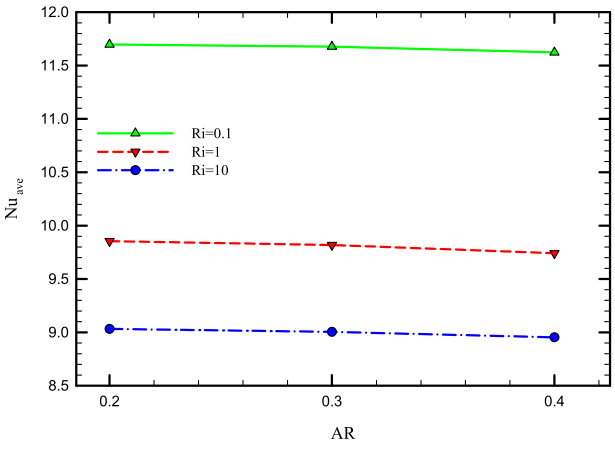

$\phi = 2\%$

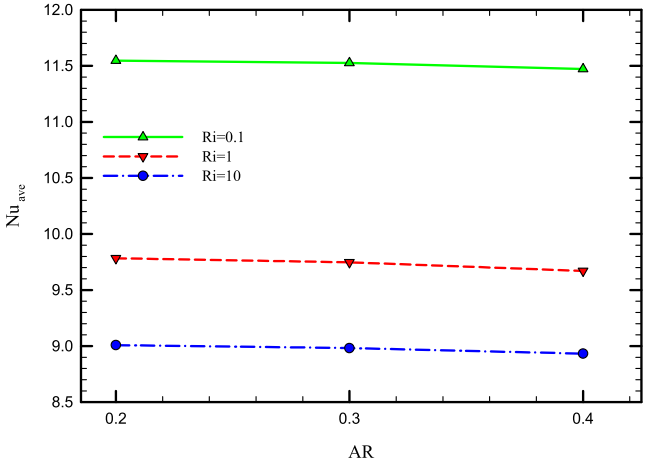

$\phi = 1\%$

Fig. 19 (*continued*)

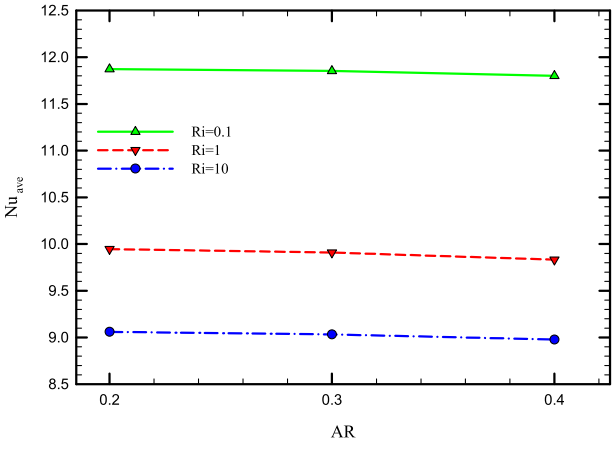

$\phi = 3\%$

Fig. 19 (*continued*)

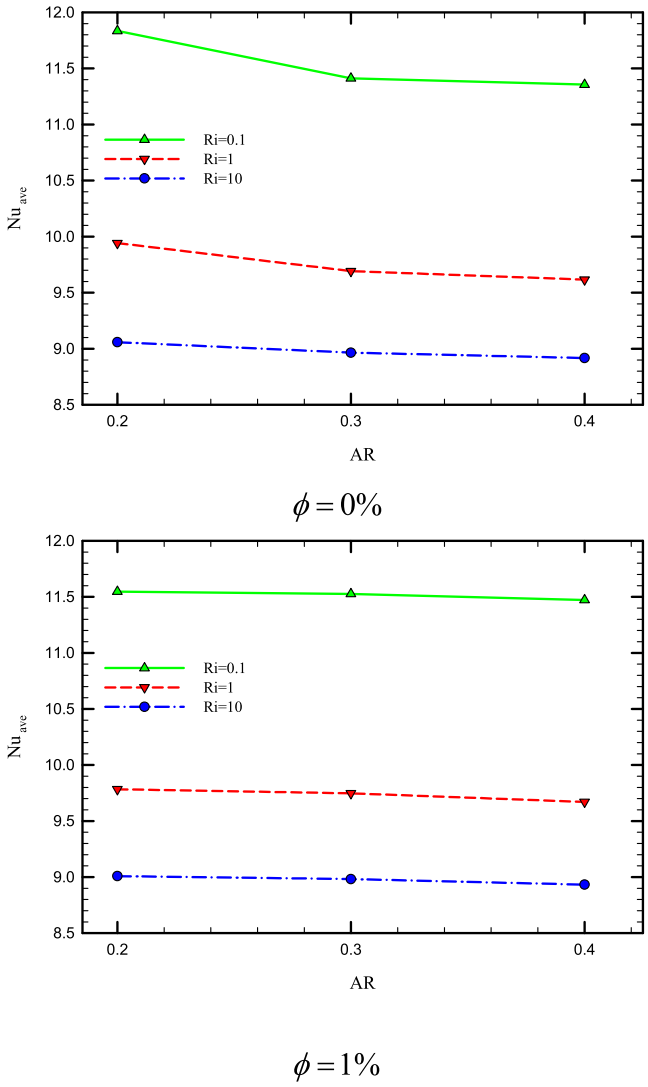

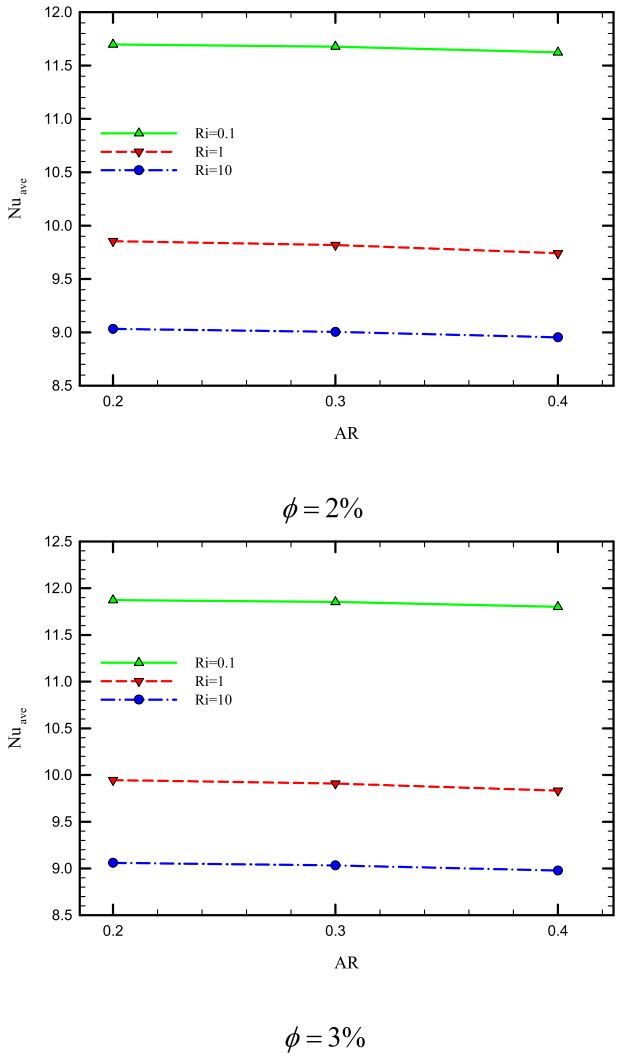

Fig. 20 Nu_{ave} versus AR in case c in different Richardson numbers.

Fig. 20 (*continued*)

Declaration of Competing Interest

The authors declare that they have no known competing financial interests or personal relationships that could have appeared to influence the work reported in this paper.

Acknowledgement

The authors are thankful to the Russian Government and Research Institute of Mechanical Engineering. Department of Vibration Testing and Equipment Condition Monitoring, South Ural State University, Lenin prospect 76, Chelyabinsk, 454080, Russian Federation for their support to this work.

References

[1] Y. Fu, H. Chen, R. Guo, Y. Huang, M.R. Toroghinejad, Extraordinary strength-ductility in gradient amorphous structured Zr-based alloy, J. Alloy. Compd. 888 (2021) 161507, https://doi.org/10.1016/j.jallcom.2021.161507.

[2] Q. Zhong, J. Yang, K. Shi, S. Zhong, L. Zhixiong, et al, Event-Triggered H∞ Load Frequency Control for Multi-Area Nonlinear Power Systems Based on Non-Fragile Proportional Integral Control Strategy, IEEE Transactions on Intelligent Transportation Systems. (2021), https://doi.org/10.1109/TTTS.2021.3110759.

[3] P. Wang, S.-Z. Wang, Y.-R. Kang, Z.-S. Sun, X.-D. Wang, Y.u. Meng, M.-H. Hong, W.-F. Xie, Cauliflower-shaped Bi2O3–ZnO heterojunction with superior sensing performance towards ethanol, J. Alloy. Compd. 854 (2021) 157152, https://doi.org/10.1016/j.jallcom.2020.157152.

[4] L. Hu, X. Huang, S. Zhang, X. Chen, X. Dong, H. Jin, et al, MoO.sub.3 structures transition from nanoflowers to nanorods and their sensing performances, Journal of materials science. Materials in electronics 32 (19) (2021) 23728, https://doi.org/10.1007/s10854-021-06464-7.

[5] H. Wu, F. Zhang, Z. Zhang, Droplet breakup and coalescence of an internal-mixing twin-fluid spray, Phys. Fluids 33 (1) (2021) 013317, https://doi.org/10.1063/5.0030777.

[6] X. Zhang, Y. Tang, F. Zhang, C. Lee, A Novel Aluminum-Graphite Dual-Ion Battery, Adv. Energy Mater. 6 (11) (2016) 1502588, https://doi.org/10.1002/aenm.201502588.

[7] X. Tong, F. Zhang, B. Ji, M. Sheng, Y. Tang, Carbon-Coated Porous Aluminum Foil Anode for High-Rate, Long-Term

Cycling Stability, and High Energy Density Dual-Ion Batteries, Advanced materials (Weinheim) 28 (45) (2016) 9979–9985, https://doi.org/10.1002/adma.201603735.
[8] B. Ji, F. Zhang, X. Song, Y. Tang, A Novel Potassium-Ion-Based Dual-Ion Battery, Advanced materials (Weinheim) 29 (19) (2017) 1700519, https://doi.org/10.1002/adma.201700519.
[9] X. Wang, C. Li, Y. Zhang, Z. Said, S. Debnath, S. Sharma, et al, Influence of texture shape and arrangement on nanofluid minimum quantity lubrication turning, The International Journal of Advanced Manufacturing Technology (2021), https://doi.org/10.1007/s00170-021-08235-4.
[10] Gorgani, Hamid Haghshenas, Peyman Maghsoudi, and Sadegh Sadeghi. "An innovative approach for study of thermal behavior of an unsteady nanofluid squeezing flow between two parallel plates utilizing artificial neural network." European Journal of Sustainable Development Research 3, no. 1 (2019): em0069. https://doi.org/10.20897/ejosdr/3935
[11] Shahriari, Gholamreza, Peyman Maghsoudi, and Sadegh Sadeghi. "Impact of Viscous Dissipation on Temperature Distribution of a Two-dimensional Unsteady Graphene Oxide Nanofluid Flow between Two Moving Parallel Plates Employing Akbari-Ganji Method." European Journal of Sustainable Development Research 2, no. 2 (2018): 24. https://doi.org/10.20897/ejosdr/81574
[12] F. Arslan, LMS Algorithm for Adaptive Transversal Equalization of a Linear Dispersive Communication Channel, Review of Computer Engineering Research 7 (2) (2020) 73–85, https://doi.org/10.18488/journal.76.2020.72.73.85.
[13] A. Talavari, B. Ghanavati, A. Azimi, S. Sayyahi, Pvdf/ Mwcnt Hollow Fiber Mixed Matrix Membranes for Gas Absorption by Al2o3 Nanofluid, Progress in Chemical and Biochemical Research 4 (2) (2021) 177–190, https://doi.org/10.22034/pcbr.2021.270178.1177.
[14] D. Sezavar, M. Miri, Investigating Fluid Mixing in Electro-Osmotic Flow through Passive Micro-Mixers Having Square and Triangle Barriers, Int. J. Adv. Biol. Biomed. Res. 2 (12) (2014) 2940–2948.
[15] A. Li, X. Mu, X. Zhao, J. Xu, M. Khayatnezhad, R. Lalehzari, Developing the non-dimensional framework for water distribution formulation to evaluate sprinkler irrigation*, Irrig. and Drain. 70 (4) (2021) 659–667.
[16] Baghernejad, Bita, and Mostafa Rostami Harzevili. "Nano-Cerium Oxide/Aluminum Oxide: An Efficient and Useful Catalyst for the Synthesis of Tetrahydro[a]Xanthenes-11-One Derivatives." Chemical Methodologies 5, no. 2 (2021): 90-95. DOI: 10.22034/chemm.2021.119641
[17] Krdžalić, Amina, and Lejla Hodžić. "Sustainable engineering challenges towards Industry 4.0: A comprehensive review." Sustainable Engineering and Innovation, ISSN 2712-0562 1, no. 1 (2019): 1-23.
[18] Y. Wang, B. Ruhani, M.A. Fazilati, S.M. Sajadi, A. Alizadeh, D. Toghraie, Experimental analysis of hollow fiber membrane dehumidifier system with SiO2/CaCl2 aqueous desiccant solution, Energy reports 7 (2021) 2821–2835.
[19] M. Salehi, P. Heidari, B. Ruhani, A. Kheradmand, S. Purcar, S. Căprărescu, Theoretical and Experimental Analysis of Surface Roughness and Adhesion Forces of MEMS Surfaces Using a Novel Method for Making a Compound Sputtering Target, Coatings 11 (12) (2021) 1551.
[20] R. Ruhani, A. Abidi, A. Kadhim Hussein, O. Younis, M. Degani, M. Sharifpur, Numerical simulation of the effect of battery distance and inlet and outlet length on the cooling of cylindrical lithium-ion batteries and overall performance of thermal management system, J Energy Storage 45 (2022) 103714.
[21] M.F. Gözükızıl, pH effect on structural, morphological and optical properties of ZnO thin films produced by chemical bath deposition method, European Chemical Bulletin 9 (10) (2020) 335–338.
[22] V. Bakhtadze, V. Mosidze, T. Machaladze, N. Kharabadze, D. Lochoshvili, M. Pajishvili, et al, Activity of Pd-MnOx/CORDIERITE (Mg, Fe) 2Al4Si5O18) catalyst for carbon monoxide oxidation, European Chemical Bulletin 9 (2) (2020) 75–77.
[23] M. Bashirzadeh, Green synthesis of quinoxaline derivatives at room temperature in ethylene glycol with H_2SO_4/SiO_2 catalyst, European Chemical Bulletin 9 (1) (2020) 33–37.
[24] S. Mirmasoumi, A. Behzadmehr, Effect of nanoparticles mean diameter on mixed convection heat transfer of a nanofluid in a horizontal tube, Int. J. heat fluid flow 29 (2008) 557–566.
[25] S.M. Aminossadati, B. Ghasemi, A numerical study of mixed convection in a horizontal channel with a discrete heat source in an open cavity, Eur. J. Mech. 28 (4) (2009) 590–598.
[26] K.-C. Wong, N.H. Saeid, Numerical study of mixed convection on jet impingement cooling in an open cavity filled with porous medium, Int. Commun. Heat Mass Transf. 36 (2009) 155–160.
[27] E. Abu-Nada, A.J. Chamkha, Mixed convection flow in a lid-driven inclined square enclosure filled with a nanofluid, Eur. J. Mech. 29 (2010) 472–482.
[28] A.H. Mahmoudi, M. Shahi, A.M. Shahedin, N. Hemati, Numerical modeling of natural convection in an open cavity with two vertical thin heat sources subjected to a nanofluid, Int. Commun. Heat Mass Transf. 38 (2011) 110–118.
[29] M.M. Rahman, R. Saidur, N.A. Rahim, Conjugated effect of joule heating and magneto-hydrodynamic on double-diffusive mixed convection in a horizontal channel with an open cavity, Int. J. Heat Mass Transf. 54 (2011) 3201–3213.
[30] P. Barnoon, D. Toghraie, M. Salarnia, A. Karimipour, Mixed thermomagnetic convection of ferrofluid in a porous cavity equipped with rotating cylinders: LTE and LTNE models, J Therm Anal Calorim 146 (1) (2021) 187–226.
[31] P. Barnoon, M. Ashkiyan, Magnetic field generation due to the microwaves by an antenna connected to a power supply to destroy damaged tissue in the liver considering heat control, J Magn Magn Mat 513 (2020) 167245, https://doi.org/10.1016/j.jmmm.2020.167245.
[32] M. Mahmoodi, Numerical simulation of free convection of a nanofluid in L-shaped cavities, Int. J. Therm. Sci. 50 (9) (2011) 1731–1740.
[33] G. Mahmoudi, B. Ghasemi, G. Mahmoudi, B. Ghasemi, "Effect of a baffle on mixed convection heat transfer from an open cavity with heat sources, Aerospace mechanics journal. 8 (2012) 45–56.
[34] S. Parvin, R. Nasrin, Effects of Reynolds and Prandtl number on mixed convection in an octagonal channel with a heat-generating hollow cylinder, J. Sci. Res. 4 (2) (2012) 337, https://doi.org/10.3329/jsr.v4i2.8142.
[35] S. Mojumder, S. Saha, M. Rizwanur Rahman, M.M. Rahman, K.M. Rabbi, T.A. Ibrahim, Numerical study on mixed convection heat transfer in a porous L-shaped cavity, Eng. Sci. Technol. an Int. J. 20 (1) (2017) 272–282.
[36] S.M. Sebdani, M. Mahmoodi, S.M. Hashemi, Effect of nanofluid variable properties on mixed convection in a square cavity, Int. J. Therm. Sci. 52 (2012) 112–126.
[37] S. Parvin, R. Nasrin, M.A. Alim, N.F. Hossain, Double diffusive natural convective flow characteristics in a cavity, Procedia Eng. 56 (2013) 480–488.
[38] G.A. Sheikhzadeh, H. Ehteram, A. Aghaei, Numerical study of natural convection in a nanofluid filled enclosure with central heat source and presenting correlations for Nusselt number, Modares Mech. Eng. 13 (2013) 62–74.
[39] M.A. Mansour, A.Y. Bakier, M.A.Y. Bakier, Natural convection of the localized heat sources of T-shaped nanofluid-filled enclosures, Am. J. Eng. Res. 2 (2013) 49–61.

[40] A.A. Abbasian Arani, A.Z. Maghsoudi, A.H. Niroumand, S.M. E. Derakhshani, Study of nanofluid natural convection in an inclined L-shaped cavity, Sci. Iran. 20 (2013) 2297–2305.
[41] M. Sheikholeslami, M. Gorji-Bandpy, S. Soleimani, Two phase simulation of nanofluid flow and heat transfer using heatline analysis, Int. Commun. Heat Mass Transf. 47 (2013) 73–81.
[42] M.A.Y. Bakier, Flow in open C-shaped cavities: How far does the change in boundaries affect nanofluid?, Eng Sci. Technol. an Int. J. 17 (2014) 116–130.
[43] R. Nasrin, M.A. Alim, Heat transfer performance of nanofluid in a complicated cavity due to Prandtl number variation, Procedia Eng. 90 (2014) 377–382.
[44] M.H. Esfe, M. Akbari, A. Karimipour, M. Afrand, O. Mahian, S. Wongwises, Mixed-convection flow and heat transfer in an inclined cavity equipped to a hot obstacle using nanofluids considering temperature-dependent properties, Int. J. Heat Mass Transf. 85 (2015) 656–666.
[45] Z. Naumann, L. Schiller, A drag coefficient correlation, Z Ver Deutsch Ing 77 (1935) 318–323.
[46] E. Abu-Nada, Z. Masoud, A. Hijazi, Natural convection heat transfer enhancement in horizontal concentric annuli using nanofluids, Int. Commun. Heat Mass Transf. 35 (2008) 657–665.
[47] H.C. Brinkman, The viscosity of concentrated suspensions and solutions, J. Chem. Phys. 20 (1952) 571.
[48] Alinia, D. D. Ganji, and M. Gorji-Bandpy, ‘‘Numerical study of mixed convection in an inclined two sided lid driven cavity filled with nanofluid using two-phase mixture model,” Int. Commun. Heat Mass Transf., 38 (2011) 1428–1435
[49] T. Tjahjono, M. Elveny, S. Chupradit, D. Bokov, H.T. Hoi, M. Pandey, Role of cryogenic cycling rejuvenation on flow behavior of ZrCuAlNiAg metallic glass at relaxation temperature, Trans Indian Inst Met 74 (12) (2021) 3241–-3247.
[50] J. Qaderi, A brief review on the reaction mechanisms of CO2 hydrogenation into methanol, Int j innov res. sci stud 3 (2) (2020) 33–40.
[51] V.G. Shtamburg, V.V. Shtamburg, A.A. Anishchenko, S.V. Shishkina, I.S. Konovalova, A.V. Mazepa, Interaction of ninhydrin with N-hydroxyurea and N-alkoxyureas in acetic acid, European Chemical Bulletin 9 (5) (2020) 125–131.
[52] A. Mezrhab, S. Amraqui, C. Abid, Modelling of combined surface radiation and natural convection in a vented ‘‘T” form cavity, Int J Heat and Fluid Flow 31 (1) (2010) 83–92.
[53] A. Kasaeipoor, B. Ghasemi, S.M. Aminossadati, Convection of Cu-water nanofluid in a vented T-shaped cavity in the presence of magnetic field, Int J Therm Sci 94 (2015) 50–60.
[54] F. Selimefendigil, H.F. Öztop, Impact of a rotating cone on forced convection of Ag-MgO/water hybrid nanofluid in a 3D multiple vented T-shaped cavity considering magnetic field effects, J Therm Analy Calor 143 (2) (2021) 1485–1501.
[55] K. Zeng, K. Hachem, M. Kuznetsova, S. Chupradit, C.H. Su, H.C. Nguyen, et al, Molecular dynamic simulation and artificial intelligence of lead ions removal from aqueous solution using magnetic-ash-graphene oxide nanocomposite. *Journal of Molecular Liquids*, J Mol Liquids 118290 (2021).
[56] Y. Shang, R.B. Dehkordi, S. Chupradit, D. Toghraie, A. Sevbitov, M. Hekmatifar, et al, The Computational Study of Microchannel Thickness Effects on H2O/CuO Nanofluid Flow with Molecular Dynamics Simulations, J Mol Liq 118240 (2021).
[57] S. Chupradit, D.O. Bokov, W. Suksatan, M. Landowski, D. Fydrych, M.E. Abdullah, et al, Pin Angle Thermal Effects on Friction Stir Welding of AA5058 Aluminum Alloy: CFD Simulation and Experimental Validation, Materials 14 (24) (2021) 7565.
[58] S. Chupradit, A.T. Jalil, Y. Enina, D.A. Neganov, M.S. Alhassan, S. Aravindhan, et al, Use of Organic and Copper-Based Nanoparticles on the Turbulator Installment in a Shell Tube Heat Exchanger: A CFD-Based Simulation Approach by Using Nanofluids, J Nanomater (2021) 3250058.
[59] S. Yang, S.A. Jasim, D. Bokov, S. Chupradit, A.T. Nakhjiri, A. S. El-Shafay, Membrane distillation technology for molecular separation: a review on the fouling, wetting and transport phenomena, J Mol Liq (2021) 118115.
[60] Q.H. Pham, S. Chupradit, G. Widjaja, M.S. Alhassan, R. Magizov, Y.F. Mustafa, et al, The effects of Ni or Nb additions on the relaxation behavior of Zr55Cu35Al10 metallic glass, Materials Today Communications 29 (2021) 102909.
[61] M.A. El-Shorbagy, F. Eslami, M. Ibrahim, P. Barnoon, W.F. Xia, D. Toghraie, Numerical investigation of mixed convection of nanofluid flow in a trapezoidal channel with different aspect ratios in the presence of porous medium, Case Studies in Therm Eng 25 (2021) 100977.